

A Global High-Resolution Hydrological Model to Simulate the Dynamics of Surface Liquid Reservoirs: Application on Mars

Alexandre Gauvain¹, François Forget¹, Martin Turbet^{1,2}, Jean-Baptiste Clément¹, Lucas Lange¹, and Romain Vandemeulebrouck¹

¹Laboratoire de Météorologie Dynamique, CNRS, Sorbonne Université, Paris, France

²Laboratoire d'Astrophysique de Bordeaux, Université de Bordeaux, Bordeaux, France

Correspondence: Alexandre Gauvain (alexandre.gauvain@lmd.ipsl.fr, alexandre.gauvain.ag@gmail.com)

Abstract. Surface runoff shapes planetary landscapes, but global hydrological models often lack the resolution and flexibility to simulate dynamic surface water bodies beyond Earth. Recent studies of Mars have revealed abundant geological and mineralogical evidence for past surface water, including valley networks, crater lakes, deltas and possible ocean margins dating from late Noachian to early Hesperian times. These features suggest that early Mars experienced periods allowing liquid water stability, runoff and sediment transport. To investigate where surface water could accumulate and how it may have been redistributed, we developed a global high-resolution (km-scale) surface hydrological model. The model uses a pre-computed hydrological database that maps topographic depressions, their spillover points, hierarchical connections between basins, and lake volume-area-elevation relationships. This database approach greatly accelerates simulations by avoiding repeated geomorphic processing. The model dynamically forms, grows, merges and dries lakes and putative seas without prescribing fixed coastlines, by transferring water volumes between depressions according to their storage capacities and overflow rules. We explore model behavior over the present-day Mars' topography measured by MOLA (Mars Orbiter Laser Altimeter) topography for a range of evaporation rates (from 0.1 m/yr to 10 m/yr) and total water inventories expressed as Global Equivalent Layer (from 1 mGEL to 1000 mGEL). 48 Simulations are iterated to reach the steady state. The model outputs the extent and depth of surface water bodies and identifies main drainage pathways using overflow fluxes as runoff indicators. Results show a transition toward a contiguous northern ocean between low (1-10 m) GEL values and increasing concentration of water in northern lowlands and major impact basins at higher GEL. We discuss the model's limitations, including its dependence on topography and the absence of subsurface flows, and propose future improvements. This framework provides a quantitative tool to link preserved geomorphology with plausible past hydrological states. Future work will couple the model with a 3D global climate model into a Planetary Evolution Model (PEM) to study transient water redistribution and climate-hydrology feedbacks.

1 Introduction

Surface runoff is a key process in the interaction between climate, hydrology and geomorphology, shaping planetary landscapes (Salles et al., 2023, 2020). On Earth, several global hydrological models have been developed to study the water cycle and its interactions with the climate. However, these global models typically operate at low resolution, and representing hydrological processes at higher resolution remains a significant challenge (van Jaarsveld et al., 2025). Additionally, these models are typically solved only over the continental domain, with oceans prescribed as fixed boundary conditions rather than being dynamically simulated (Sood et al., 2015). While Earth-based models are capable of simulating the dynamic evolution of continental water bodies in response to climatic changes, their direct application to other planets is limited, since the presence, extent, and variability of oceans or large lakes over paleoclimatic timescales remain highly uncertain.

On Mars, geomorphological evidence of ancient fluvial activity is often preserved in far greater spatial detail than can be resolved by existing global hydrological models developed for Earth. This discrepancy further limits the direct application of such models in planetary studies. High-resolution observations reveal extensive evidence for past surface water flow (Carr and Clow, 1981; Seybold et al., 2018). Valley networks are much more numerous than previously thought, with higher drainage densities and strong evidence of sustained precipitation and surface runoff (Hynek et al., 2010). Detailed geomorphological analyses suggest that many valleys were carved by surface runoff producing V-shaped profiles, and subsequently modified by sapping processes that widened their cross-sections (Williams and Phillips, 2001; Irwin et al., 2005a). Estimated formative discharges for some Martian valleys are comparable to — and in some cases exceed — those of terrestrial precipitation-fed networks, consistent with episodic flood-like flows (Kite et al., 2019; Irwin et al., 2005a). Additional evidences point to larger bodies of water in Mars' past. Paleoshorelines and the distribution of deltas in the northern lowlands have been interpreted as indicating ancient oceans and large lakes (Di Achille and Hynek, 2010; Zuber, 2018; Li et al., 2025; Perron et al., 2007; Ivanov et al., 2017; Sholes et al., 2021; Citron et al., 2018; Head et al., 1999). The identification of open- and closed-basin lakes (Goudge et al., 2016; Fassett and Head, 2008) highlights the role of topographic depressions/craters in capturing and storing water. These lakes often exhibit inlet and outlet valleys, providing evidence of hydrological connectivity. Within craters and along the dichotomy boundary (transition between the old, high, cratered southern highlands and the younger, low northern plains), numerous preserved deltas attest to sustained sediment transport and deposition into standing water bodies (Fassett and Head, 2005; Palucis et al., 2014; Di Achille and Hynek, 2010). The widespread occurrence of hydrated minerals — including phyllosilicates, hydrated sulfates and hydrated silica — provides further evidence that liquid water was present on early Mars (Bibring et al., 2006; Carter et al., 2015; Ehlmann et al., 2011; Beck et al., 2025).

Despite this quantity of geomorphological and mineralogical evidences, the origin and maintenance of Martian fluvial activity remain debated and multiple processes may have contributed to valley network formation (Bouley et al., 2009). Proposed mechanisms include precipitation-fed surface runoff during transient warm/wet intervals (Craddock and Howard, 2002; Irwin et al., 2005b; Mangold et al., 2004), prolonged or episodic water flow (Carr and Malin, 2000), groundwater sapping possibly sustained by geothermal or magmatic activity (Carr and Chuang, 1997; Williams and Phillips, 2001; Carr and Malin, 2000;

Malin and Carr, 1999; Morgan and Head, 2009; Wordsworth et al., 2013), and subglacial or snowmelt-driven processes in colder climates (Grau Galofre et al., 2020).

To resolve these questions, it is critical to identify where water could accumulate and act as active reservoirs within Mars' hydrological cycle. Mapping the locations and sizes of possible surface water bodies, and quantifying exchanges between surface and atmosphere, are necessary steps to use geomorphological observations to constrain climatic conditions (Matsubara et al., 2011; Kamada et al., 2020, 2021; Boatwright and Head, 2019). To understand the climate responsible for the formation of water-related geomorphological features – such as valley networks, lakes, oceans and sedimentary deposits – a global high-resolution hydrological model is needed to simulate the surface water distribution and compare it with the observed geomorphological features. This type of hydrological model will provide a realistic distribution of surface water bodies, which can be used as input for 3D Global Climate Models (GCMs) to study the interactions between climate and hydrology (e.g., Turbet and Forget, 2021; Wordsworth et al., 2015).

This paper presents a new global high-resolution hydrological model based on the depression hierarchy and flow-routing concepts introduced by Barnes et al. (2021). The model is designed to simulate the spatial distribution, storage, and connectivity of surface water reservoirs at the planetary scale for a given global topography. This focus on global organization and long-term equilibrium behavior distinguishes our approach from most existing terrestrial hydrological models (graph-based models), which are generally developed for local to regional applications. Sequential depression-filling methods (e.g. Noel et al. (2021)) focus on event-based hydrological connectivity within individual catchments. Wetland ponding models such as WDPM Shook et al. (2021) primarily target low-relief environments and local storage dynamics. Hydrodynamic models like GraphFlood Gailleton et al. (2024) resolve two-dimensional surface flow at high spatial and temporal resolution. In contrast, our framework explicitly conserves surface water mass at the scale of the entire planet and redistributes water volumes through a pre-computed hierarchical network of topographic depressions. The model efficiently captures the large-scale structure and long-term equilibrium states of lakes, seas, and potential oceans. This makes it particularly well suited for investigating planetary surface hydrology, such as that of early Mars.

The first section describes the model assumptions and framework, particularly the use of a hierarchical depression graph (Barnes et al., 2020), the construction of the hydrological database and pre-computed hydrological functions. The implementation of the model is then explained, covering the algorithms for water overflow, evaporation, and the iterative scheme for reaching steady state. Then we present an application on Mars by using its current high-resolution topographic map (Smith et al., 2001, 1999). This section details the topographic data used to construct the hydrological database and the focused area chosen to present the results. The results' section analyze the model outputs, such as water depth, volume distribution and flow pathways. Finally, the discussion highlights the current model limitations, including its dependence on topography and the absence of subsurface flows, and proposes future improvements.

2 Model implementation

2.1 General model description

This hydrological model is designed to simulate the routing and accumulation of surface water over a given topography. Its core principle is that water flows across the landscape until it encounters depressions where it can be stored, allowing for the formation of lakes or oceans. A key feature of the model is that these lakes/oceans are not fixed boundaries: they can completely evaporate under arid conditions and reappear during wetter periods. When a lake reaches its maximum storage capacity, the model transfers the overflow to downstream depressions. This mechanism enables the transfer of water volumes between reservoirs provides a way to trace drainage pathways and reconstruct watercourses. To simulate these dynamics efficiently, the model makes several simplifying assumptions. In principle, surface-water flow is governed by the conservation of mass and momentum equations integrated overflow depth. However, solving these equations at high resolution and over large domains is computationally prohibitive. Instead, our approach assumes that water follows the steepest topographic slope until it reaches an unfilled depression.

The hydrological model is based on the existing frameworks of Barnes et al. (2020, 2021) and Callaghan and Wickert (2019). This framework is specifically designed to handle complex terrains with numerous depressions, like craters for instance (Figure 1a). It uses a binary tree data structure, known as the depression hierarchy, where each node represents either a watershed of a depression ("leaf" depression) or a meta-depression formed by the merging of two filled depressions (Figure 1b). The depressions are interconnected in a network that defines the water flow paths within the binary tree (Figure 1c). This structure significantly enhances computational efficiency, as the connections between depressions are only determined once during the pre-processing stage. Additionally, pre-computed functions link the lake elevation, water volume, and lake area for each depression, enabling quick estimation of lake surface or elevation from water volume. All of this information is gathered in a hydrological database that will be described in Section 2.2. The implementation of the hydrological model is described in Section 2.3.

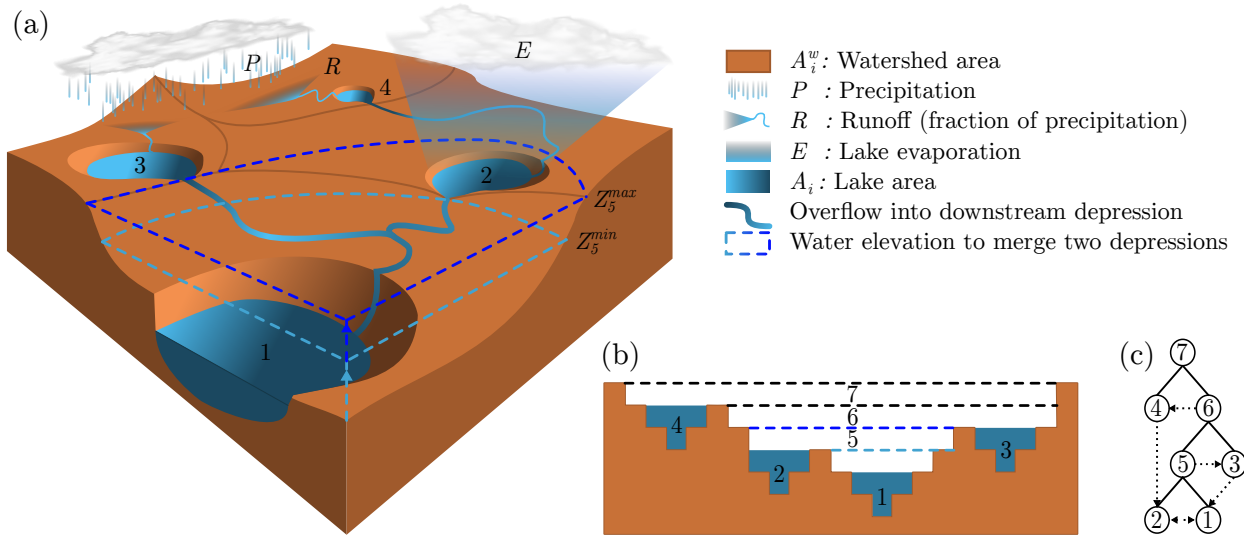


Figure 1. Representation of the water cycle on a conceptual topography with 4 leaf depressions. (a) 3D block represents the water flow from upstream to downstream. The links between the depressions, which represent streams, are symbolized by full blue curves. The sky blue dotted line represents the lake elevation where a depression No.1 can merge with a depression No.2 and create a new depression No.5. The dark blue dotted line represents the lake elevation where the depression No.5 merge with the depression No.3. The merge lines (blue and black dotted lines) are projected on the cross-section (b) of the 3D block diagram. (b) The dashed lines represent the minimum and maximum elevation limits of the depressions. (c) Binary tree of the depression hierarchy. Nodes No.1-4 are leaf depressions and nodes No.5-7 are meta-depressions. The black lines represent the merge into a new depression. The dotted arrows show the link with downstream depression. Adapted from Barnes et al. (2020).

A word of caution: the model is originally designed for watershed-scale simulations, and a key limitation for its planet-scale applicability is that we assume that water transfer between depressions occurs instantaneously. This simplification may lead to a slight underestimation of evaporation during transfer and neglects potential transient storage effects. Furthermore, each node in the binary tree represents the watershed of a depression with its own storage capacity, meaning that intra-watershed water routing is not explicitly simulated. Infiltration and subsurface flow processes are also not included at this stage of model development. Some of these limitations can be mitigated through post-processing, as described in Section 2.4.

2.2 Pre-computed hydrological database

The hydrological database aims to store all the information derived from the high resolution map that needs to be computed only once. This approach ensures computational efficiency, as the model only needs to load and apply the pre-computed database. To build this hydrological database, we used the Depression Hierarchy algorithm (Barnes et al., 2020) to calculate the binary

tree (Figure 1c, Section 2.2.1) and we pre-computed the depression information (Section 2.2.2) and functions that establish the link between volume lake, elevation lake and surface area lake for each depression (Section 2.2.3). All the information saved in the hydrologic database are listed in the Table 1.

Table 1. Maps and parameters saved in the hydrological database (NetCDF file). Parameters are divided into four parts: (1) Maps, (2) Depression Hierarchy Graph (Section 2.2.1), (3) Depression Information (Section 2.2.2) and (4) Hydrological Functions (Section 2.2.3). Each depression is referenced by a unique identifier (ID).

	Parameter	Description	Unit
Maps	DEM	Digital Elevation Model	m
	$Watershed$	Label map of the leaf depression watershed	ID
Depression Hierarchy Graph	i	Depression	ID
	P_i	Parent of the depression i	ID
	S_i	Sibling depression	ID
	D_i	Downstream depression	ID
	R_i	Right child depression	ID
	L_i	Left child depression	ID
Depression Information	Z_i^{max}	Elevation of the spillover point	m
	Z_i^{min}	Elevation of the merge point of the children	m
	A_i^w	Watershed area	m^2
	V_i^{max}	Maximum water volume	m^3
	λ_i^{sp}	Longitude of the spillover point	degree
	φ_i^{sp}	Latitude of the spillover point	degree
	λ_i^{min}	Minimum longitude of watershed extent	degree
	λ_i^{max}	Maximum longitude of watershed extent	degree
	φ_i^{min}	Minimum latitude of watershed extent	degree
φ_i^{max}	Maximum latitude of watershed extent	degree	
Hydrological Functions	$V_i^l = f_i(Z_i^l)$	Lake volume as a function of lake elevation	m^3
	$A_i^l = f_i(Z_i^l)$	Lake area as a function of lake elevation	m^2

2.2.1 Hierarchical depression graph

The Depression Hierarchy (DH) algorithm (Barnes et al., 2020) is a powerful method for analyzing depressions from a Digital Elevation Model (DEM) to create a hierarchical depression graph across complex landscapes. The algorithm is divided into four stages: (1) ocean identification, (2) pit cell identification, (3) depression assignment, and (4) hierarchy construction. As mentioned previously, the model must allow water bodies to evolve dynamically. In the original workflow developed for Earth, an ocean identification step is used to define which cells are treated as ocean in order to initialize the DH construction. This

step does not impose a fixed ocean elevation, but rather specifies the starting locations from which pit cells are identified and connected. In our case, to avoid prescribing any predefined ocean and to allow for the possible emergence of a planetary-scale ocean through water redistribution, the ocean identification threshold was set to the highest cell in the DEM. Algorithmically, this choice simply initializes the DH construction from that location, without constraining the subsequent evolution of water bodies. The process begins by computing the water flow direction using the simple D8 algorithm (O’Callaghan and Mark, 1984; Barnes, 2016). For each cell of the DEM, the water flow direction is defined by following the steepest slope calculated from the 8 neighboring cells. This flow direction map allows the identification of the pit cells which are DEM cells without an outlet, surrounded by eight neighboring cells with equal or higher altitude. After locating these pit cells, the algorithm marks each DEM cell with the identifier of the pit cell that it drains into, following the flow direction map. This process delineates the watershed area for each depression. The Depression Hierarchy algorithm gives a label map of the depression identifiers (ID) representing the watershed area for each leaf depression. This map is saved in the hydrological database. At this step, the algorithm fills each depression until the spillover point, which is the lowest elevation point where water can overflow into neighboring terrain (Barnes et al., 2014). The spillover point of the watershed is identified as being the lowest elevation point on the watershed boundary. Then, a hierarchical structure is built on how the depressions are nested or connected to another one. Smaller depressions that fill first may overflow into adjacent depressions, establishing a parent-child relationship. The algorithm then links each depression to its parent depression through its spillover point, creating a binary tree where depressions are ranked according to their order of filling. Each depression i has a parent depression P_i , a sibling depression S_i and a targeted downstream depression D_i . The meta-depression i (merge of two depressions) has a right child R_i and a left child L_i . For instance, the meta-depression No.5 (Figure 1b-c.) has the depression No.6 as parent, depression No.3 as the sibling and targeted downstream depressions, and the depressions No.1 and No.2 as right and left children. The last node at the top of the binary tree represents the whole planet. This algorithm is designed to generate a hierarchical depression graph at watershed scale. For a planetary (spherical) context, some modifications are required to ensure flow continuity across the globe. Specifically, the algorithm is adjusted to account for the east-west continuity, linking the two opposite sides of the DEM. This modification allows depressions at the interface of the DEM boundaries to be identified and connected.

2.2.2 Depression information

Once the hierarchical depression graph is established, several parameters in the hydrologic database (Table 1) are computed to characterize the depressions and the associated watershed. The maximum and minimum water elevations in the depression, Z_i^{max} and Z_i^{min} , are directly given by the depression hierarchy algorithm. Z_i^{max} corresponds to the elevation of the spillover point (Figure 1a). For the leaf depression, Z_i^{min} is the minimal elevation given by topography elevation in the watershed while, for the meta-depression, it is the elevation of the spillover point of its two child depressions ($Z_{R_i}^{max}$ and $Z_{L_i}^{max}$). Using the label map, the watershed area A_i^w , which represents the surface contributing to a given depression, can be computed by summing the depression cell areas. The maximum volume of water that each depression can contain, V_i^{max} , is computed from the elevation topography map, the watershed area and the water depth below Z_i^{max} . For the meta-depressions, V_i^{max} is computed with the water depth between Z_i^{min} and Z_i^{max} . λ_i^{sp} and φ_i^{sp} specify the coordinates (longitude and latitude) of the spillover point. λ_i^{min} ,

λ_i^{max} , φ_i^{min} and φ_i^{max} are the grid coordinates delimiting the extent of the watershed depression. These coordinates are mainly used to focus on a specific depression, decrease the computation time of constructing hydrological functions and facilitate the post-processing.

2.2.3 Pre-computed hydrological lake functions

To efficiently convert the volume stored by the depression into lake water levels or lake surface areas, we pre-computed these relationships as functions of the lake elevation. These functions characterize the evolution of three lake-related metrics: the lake volume V_i^l , the lake surface area A_i^l and the lake elevation Z_i^l . For each depression and each metric, a value is computed at every 10% of the water elevation, between Z_i^{min} and Z_i^{max} . The hydrological functions are stored as look-up tables to be linearly interpolated in the hydrological database (Table 1) and loaded by the hydrological model when the simulation starts.

A linear interpolation is used to estimate the lake area A_i and the lake elevation Z_i based on a given lake volume V_i . The algorithm searches for the appropriate interval $[V_{i,k}^l, V_{i,k+1}^l]$ in the pre-computed hydrological function such that the index k is the largest index satisfying $V_{i,k}^l < V_i \leq V_{i,k+1}^l$. Then, the interpolated values of lake area A_i and lake elevation Z_i are computed as follows:

$$A_i = A_{i,k}^l + \frac{V_i - V_{i,k}^l}{V_{i,k+1}^l - V_{i,k}^l} \times (A_{i,k+1}^l - A_{i,k}^l) \quad (1)$$

and

$$Z_i = Z_{i,k}^l + \frac{V_i - V_{i,k}^l}{V_{i,k+1}^l - V_{i,k}^l} \times (Z_{i,k+1}^l - Z_{i,k}^l) \quad (2)$$

To highlight the gain in computational efficiency provided by the pre-computed hydrological functions, we compared, in Appendix A, the results and the time taken to compute the lake area and elevation for a given water volume using our interpolation method versus a direct computation method from Fill-Spill-Merge algorithm from Barnes et al. (2021).

2.3 Hydrological model

The hydrological model governs the redistribution of excess water along the depression hierarchy graph. Using the pre-computed functions stored in the hydrological database, the model reconstructs and updates the hierarchical structure at runtime based on the parameters summarized in Table 1. For each depression i (represented by a node in the binary tree), the variables describing its hydrological state: water volume V_i , outgoing discharge Q_i^{out} , active state a_i , lake surface area A_i , and elevation Z_i are continuously updated during the simulation. The active state a_i is a flag that indicates the highest level of the depression that contains water, i.e. the leaf or meta-depression that have surface water in contact with the atmosphere. A filled depression with a filled parent depression is considered inactive ($a_i = 0$) since its water volume is not in contact with the atmosphere. On the contrary, a filled depression with an empty parent depression is considered active ($a_i = 1$) since the water is in contact with the atmosphere. Only leaf depressions can be active even if they are empty.

2.3.1 Global scheme

The hydrological model is designed to finally be coupled with a GCM to simulate the dynamic interactions between surface water and climate. In this paper, we present the hydrological model as a module that can be coupled with a GCM, but for testing purposes, we use a simplified global climate grid that provides conceptual evaporation and precipitation rates/patterns. This first approach prepares and will facilitate the future coupling of the hydrological model with a GCM, while allowing us to validate the hydrological model independently of a global climate model.

The process begins by loading the hydrological database, which contains pre-computed information about the depressions and their hierarchical relationships. Next, the model connects each leaf depression with the corresponding climate grid cell. The first step of the hydrological model is an initialization stage which can be done by two ways: (1) globally, by applying a uniform Global Equivalent Layer (*GEL*), which is injected in each leaf depression i following the equation :

$$V_i = A_i^w \times GEL \quad (3)$$

Or (2) locally, by injecting the amount of the Global Equivalent Layer of water at a specific georeferenced point (longitude and latitude coordinates) following the equation:

$$V_j = A_p \times GEL \quad (4)$$

where A_p is the area of the planet and j is the leaf depression *ID* covering the georeferenced point. Both initialization methods are used in the following application of the model on Mars (Section 3).

Then, all leaf depressions are set as active ($a_i = 1$) at the initialization step, even if they are empty. The algorithm checks if the water volume V_i of the leaf depression is higher than the maximum volume V_i^{max} and will handle the excess volumes V^{excess} . Once the excess volumes are redistributed following the recursive subroutine described in Section 2.3.2, the lake areas are computed by interpolation using the hydrological lake functions (Section 2.2.3). Then, the location and area of lakes can be used as inputs to the climate grid, indicating the percentage of water coverage for each climate grid cell. The climate grid then provides the precipitation and evaporation rates. The retrieved precipitation and evaporation data are then used to update the water distribution in the hydrological model. This iterative process continues, with the model recalculating the water surface area and feeding it back into the climate grid, ensuring a dynamic and interactive simulation of the hydrological and climatic systems.

To test and validate the hydrological model, conceptual climate scenarios, as a reference cases, are investigated with a constant evaporation rate E (ms^{-1}) and homogeneous precipitation P (ms^{-1}) of the total evaporated volume. This process allows to conserve the mass of water in the system and to reach an equilibrium of the water surface reservoirs. After the initialization step (Equation 3 or 4), the hydrological model uses an iterative scheme to reach a steady state. One iteration of the model corresponds to the following scheme. First, the potential evaporated volume V_i^{EP} (m^3) is computed for each

depression i based on its active state a_i , the evaporation rate E and water surface area A_i (m^2):

$$V_i^{Ep} = \begin{cases} A_i E \Delta t & \text{if } a_i = 1 \\ 0 & \text{if } a_i = 0 \end{cases} \quad (5)$$

where Δt is the adaptive time step (s) of the simulation. In function of the value of V_i^{Ep} and the available volume V_i , the model computes the real evaporated volume V_i^{Er} that each depression i is able to evaporate (Section 2.3.3). In the case where the available volume is lower than V_i^{Ep} , the adaptive time step Δt is decreased to ensure that the relative difference between V_i^{Ep} and V_i^{Er} is negligible (less than 1%). To ensure mass conservation, the precipitation rate P ($\text{m}\cdot\text{s}^{-1}$) is then calculated using the total of real evaporated volume V_i^{Er} and the planet area A_p :

$$P = \frac{\sum_{i=1}^N a_i V_i^{Er}}{\Delta t A_p} \quad (6)$$

Next, the water volume change ΔV_i is computed for each active depression i by combining the water balance equation (Howard, 2007; Matsubara et al., 2011, 2013) with the adaptive time step Δt :

$$\Delta V_i = \Delta t [(A_i^w - A_i) P \beta + A_i P - A_i E] \quad (7)$$

where β is the fraction of precipitation that contributes to runoff. In this conceptual study, it is assumed that there is no infiltration ($\beta = 1$). If $\Delta V_i < 0$, the absolute value of ΔV_i is evaporated from the depression following the process describes in the Section 2.3.3. Conversely, if $\Delta V_i > 0$, the depression receives the water volume ΔV_i . If $V_i + \Delta V_i$ is higher than V_i^{max} , the excess volume is redistributed following the water overflow algorithm (Section 2.3.2). Once the water volume change is processed and the water volumes V_i are updated for all depressions, the model recalculates the lake elevation Z_i and lake surface area A_i using the hydrological lake functions (Section 2.2.3). This iterative process continues until the system reaches a steady state when the water volume V_i and lake surface area A_i in each depression remains constant. More precisely, equilibrium is assumed when the relative change in water volume and surface area in each active depression between two successive iterations is less than 0.1%, and no new overflow events are triggered anywhere on the planet.

2.3.2 Overflow algorithm

The hierarchical relationship between nodes (depression, sibling, and parent nodes) governs how excess water is redistributed. The main challenge in this model is managing excess water that accumulates when a reservoir exceeds its storage capacity. The Pseudo-code 6.2 (OverflowInto) of the Fill-Spill-Merge algorithm from Barnes et al. (2021) is implemented in the hydrological model to handle this redistribution of excess water across the depression hierarchy graph. The process follows a set of rules and priorities to distribute effectively the excess water V^{excess} , based on a recursive subroutine following three successive steps :

- (1) If the water volume in the considered depression V_i is less than its maximum capacity V_i^{max} , the remaining available volume $V_i^{avail} = V_i^{max} - V_i$ is used to store a part or the entire excess volume. In case where V^{excess} is smaller than V_i^{avail} , the reservoir stores all the excess water, and V^{excess} becomes equal to 0. Conversely, when V^{excess} is larger than

V_i^{avail} , the outgoing water volume of the depression is calculated as: $V_i^{out} = V^{excess} - V_i^{avail}$ and the depression fills up ($V_i^{avail} = 0$ and $V_i = V_i^{max}$). This outgoing water volume will be redirected to another storage location according to the steps (2) and (3).

- (2) If the considered depression is full ($V_i = V_i^{max}$), the next step is to check if the redirection of the excess water to the sibling depression S_i is possible. As a reminder, the sibling depression is a neighboring depression at the same level of the hierarchy. This redirection of the excess water is only possible if the sibling has available space $V_{S_i}^{avail} > 0$ and has already water in the depression $V_{S_i} > 0$. If the water volume of the sibling depression V_{S_i} is equal to 0, then this means that the excess volume must be transferred to an active downstream depression (i.e. a depression at a lower level of the hierarchy). The excess volume is transferred to the downstream depression D_i . Depending on these conditions, the recursive process restart at the step (1) in the sibling depression S_i or downstream depression D_i with the excess volume computed in step (1).
- (3) If the volume depression V_i of the considered depression i and its sibling V_{S_i} are full, the last option is to transfer the excess water to the parent depression V_{P_i} , which is higher up in the hierarchy. The active state of the considered depression a_i and the sibling depression a_{S_i} is set to 0. The active state of the parent depression a_{P_i} switches to 1. The recursive process restarts at the step (1) in the parent depression P_i with the excess volume computed in step (1).

The excess volume of water going out from each depression is accumulated in Q_i^{out} . This recursive process continues, allowing the model to simulate water moving up within the depression hierarchy graph. The recursive loop finish when V^{excess} is equal to 0.

As in the Fill-Spill-Merge algorithm from Barnes et al. (2021), a bypass mechanism is implemented to optimize the computational efficiency of the hydrological model. For a given depression, the final depression where V^{excess} reaches zero can be stored in memory. Subsequently, if another V^{excess} is introduced into the same initial depression, the algorithm bypasses intermediate steps and directly routes the new V^{excess} to the previously identified final depression. This approach significantly reduces redundant calculations and accelerates the redistribution of water across the depression hierarchy, particularly in scenarios of repetitive water flow patterns. This option can be turned on or off in the hydrological model. The activation of this bypass mechanism have a negative impact since it does not make the overflow Q_i^{out} possible to compute. However, once the simulation has converged to a steady state with the bypass enabled, this option can be disabled for one additional iteration to accurately recalculate the overflow fluxes for each depression.

2.3.3 Evaporation algorithm

To simulate the evaporation process, the hydrological model uses a hierarchical evaporation scheme. Considering a depression i and a potential evaporated volume V_i^{Ep} (Section 2.3.1, Equation 5) in this same depression, the algorithm traverses the depression hierarchy graph by level, i.e. the depressions located below depression i (i.e., right child R_i and left child L_i , Figure 1b-c). When a sufficient amount of water is present in depression i and its underlying depressions, the real evaporated water volume V_i^{Er} equals the potential water volume to evaporate. Otherwise, when the amount of water is insufficient, the real

evaporated water volume V_i^{Er} becomes less than the potential evaporated volume V_i^{Ep} . The algorithm continues to traverse the hierarchy by level until it reaches a leaf depression with no water, or it evaporates all the potential evaporated volume V_i^{Ep} . In the model, the evaporation routine is represented as :

$$V_i^{Er} = \min \left(\sum_k V_k^E, V_i^{Ep} \right) \quad (8)$$

where $\sum_k V_k^E$ is the sum of the evaporated volume in all depressions k that are below the depression i , depression i included.

2.4 Model outputs and post-processing

The simulation outputs are saved in a NetCDF file and can be saved at each iteration, depending on the frequency specified by the user, or only at the end of the simulation. The saved data include the lake surface elevation Z_i , the area covered by the lake A_i , the volume of water stored in the depression V_i , the active state a_i (indicating whether it is active or inactive), and the water overflow Q_i^{out} for each depression. These outputs enable the reconstruction of water reservoir distributions and the analysis of hydrological flows for comparison with observations. The hydrological model outputs are then post-processed to analyze the water volume distribution, water depth and accumulated outflow in each depression. To compute the water depth, the model uses the lake elevation Z_i , the ID label map and the elevation map. The ID label map is used to identify the area covered by the depressions associated. The water depth map is then computed by subtracting the elevation of each grid cell of the depression i from the lake elevation. The water depth map provides insights into the water distribution across the planet and the topographic features of the depressions. The volume distribution map can be obtained by multiplying the water depth map by the area of each cell. The volume distribution map provides information on the amount of water stored in each depression. The accumulated outflow map is generated by mapping the overflow discharge Q_i^{out} for each depression, either normalized by the lake surface area or distributed across the contributing watershed area. While the model outputs the accumulated overflow Q_i^{out} for each depression, it does not explicitly resolve the flow pathways between depressions. To overcome this limitation and reconstruct a continuous river network, a post-processing procedure is applied. The first step consists in modifying the original topography by assigning the lake water levels Z_i to the corresponding depressions. This creates a new topographic surface where water can flow continuously across lake basins which overflow. Flat zones introduced by the filled lakes are then corrected using the 'resolve_flats' function from the Pyshed library (Bartos, 2020), allowing proper flow routing. The flow direction is computed using the D8 algorithm (O'Callaghan and Mark, 1984), and flow accumulation is then calculated following the method of Freeman (1991). Based on this accumulation map, the main drainage paths are extracted with the 'extract_river_network' function of Pyshed. Finally, the overflow discharges from the hydrological model are assigned to the extracted river channels, producing a spatially explicit reconstruction of surface water pathways. This step provides a physically consistent representation of surface runoff and facilitates comparison with observed valley networks on Mars.

3 Application on Mars

3.1 Mars topography

We used the topographic map from MOLA (Mars Orbiter Laser Altimeter Smith et al., 1999, 2001; Neumann et al., 2001) which covers all the Mars' surface with a fine resolution of 463 meters at the equator (1/128 degree per pixel, Figure 2a). This dataset provides a detailed digital elevation model (DEM) of Mars which represents approximately 1 billion cells ($23,040 \times 46,080$ cells). This high-resolution topographic data is crucial for accurately identifying depressions and their watersheds. It is clear that the MOLA topographic map does not fully represent the topography of Mars during the periods when liquid water was stable on the surface. However, this current topographic map provides, on several preserved areas, mainly in the Southern Hemisphere, a good approximation of the past topography during the Noachian periods (4.1 to 3.7 billion years ago) when most of the fluvial features were formed (Tanaka et al., 2014). While the current MOLA topographic map accurately represents present-day Mars, it does not provide a global representation of the ancient surface topography required to study early Mars hydrology. Then, we also applied our model on a reconstructed topographic map of Mars built by Bouley et al. (2016) which remove the True Polar Wander (TPW) to better represent the global hydrology on early Mars. However, this reconstructed topographic map is only available at a lower resolution of 1 pixel per degree, which limits the ability to capture fine-scale topographic features and depressions.

Despite its limitations, the topographic analysis of MOLA data has provided significant insights into the hydrological activity on Mars, revealing a variety of geomorphological features indicative of past water flow (Figure 2a). Valley networks, such as those identified by Carr and Clow (1981) and Hynek et al. (2010), suggest the presence of fluvial processes that shaped the Martian surface, with drainage densities and morphologies pointing to sustained precipitation and surface runoff. Additionally, the identification of open- and closed-basin lakes, as documented by Goudge et al. (2016) and Fassett and Head (2008), highlights the role of topographic depressions in capturing and storing water. These lakes often exhibit inlet and outlet valleys, providing evidence of hydrological connectivity. Furthermore, deltas, such as those observed by Di Achille and Hynek (2010), mark the confluence of sediment-laden streams with standing bodies of water, offering clues about sediment transport and deposition processes. Finally, potential shorelines, including the Arabia and Deuteronilus levels described by Sholes et al. (2021), suggest the existence of ancient oceans in the northern lowlands.

Additionally, the recent crater database of 2020 (Robbins and Hynek, 2012) contains more than 385,000 craters with a diameter larger than 1 km. The density of craters is not uniform across the planet, with a higher density in the Southern Hemisphere and a lower density in the Northern Hemisphere (Figure 2a). This gives insights into the minimum number of leaf depressions that can be contained in the hydrological database.

To highlight the application of our model, we first present results at the global scale, then focus on three well-studied systems: Nirgal Vallis, Jezero Crater, and Gale Crater (Figure 2b-d). Nirgal Vallis (Figure 2b) is one of the longest valley networks on Mars, extending over 700 km. Its morphology makes it an ideal case study for understanding fluvial processes and the potential for past water flow on Mars. High-resolution MOLA data enable detailed hydrological simulations within this catchment. Jezero Crater (Figure 2c) and Gale Crater (Figure 2d) are of particular interest because they are the landing sites

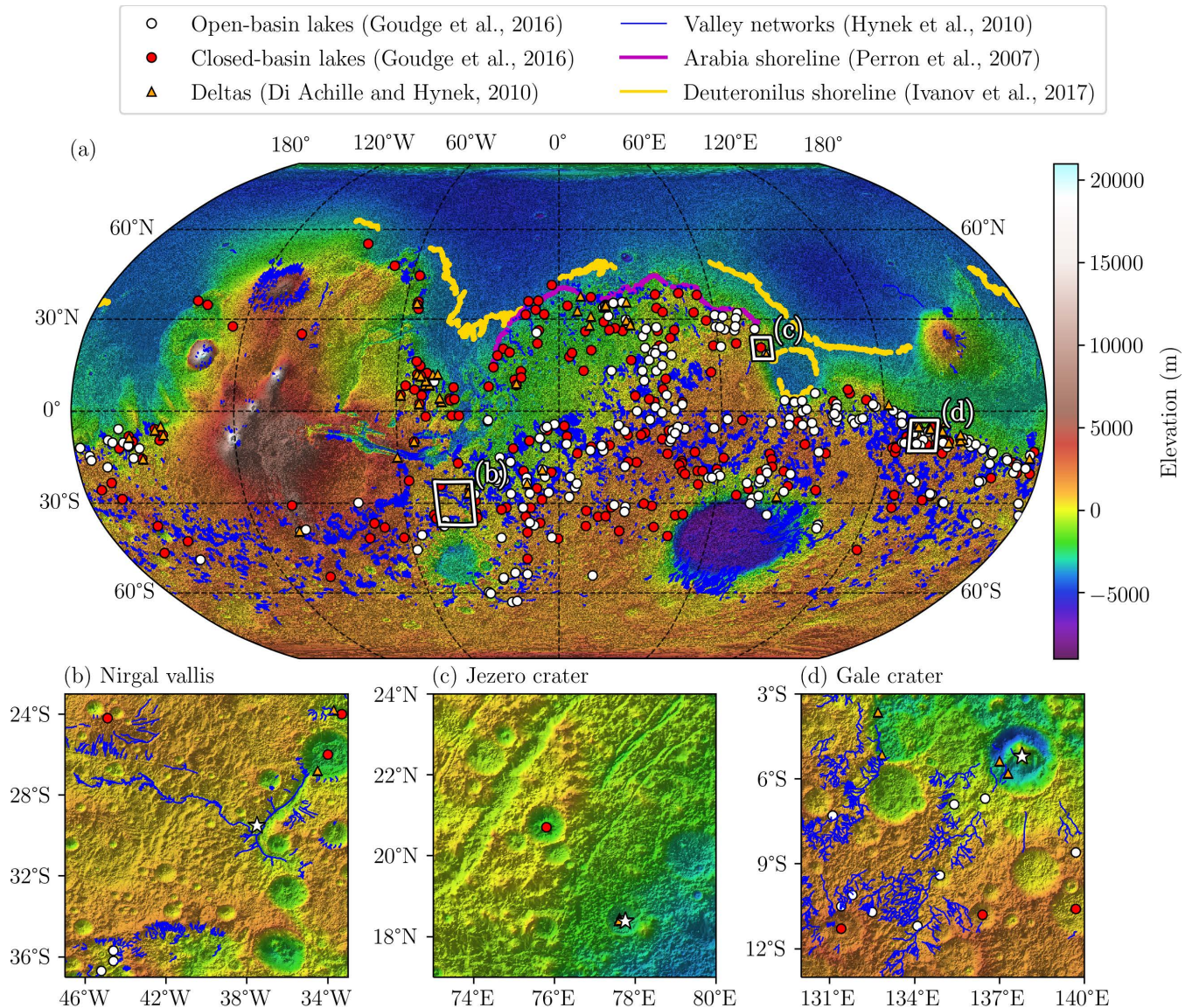


Figure 2. Mars topographic map showing the inventory of observed data relating to water flow effects. (a) Digital Elevation Model (DEM) from the Mars Orbiter Laser Altimeter (MOLA) (Smith et al., 2001; Neumann et al., 2001). The shaded relief is generated from the DEM with a sun angle of 45° from horizontal and a sun azimuth of 315° , as measured clockwise from north. The blue lines represent the valley networks (Hynek et al., 2010). The white and red dots represent open-basin and closed-basin lakes, respectively (Goudge et al., 2016). The orange triangles represent deltas (Di Achille and Hynek, 2010). The magenta and yellow lines represent respectively Arabia (Perron et al., 2007) and Deuteronilus (Ivanov et al., 2017) shorelines. The white squares are zoomed areas on Nirgal Vallis' watershed (b), Jezero' watershed (c) and Gale' watershed (d). The white stars on the zoomed areas indicate the outlets of Nirgal Vallis (b), Jezero Crater (c), and Gale Crater (d).

of the Perseverance and Curiosity rovers, respectively. Both craters host well-preserved deltas and sedimentary deposits such as conglomerates and stratified layers, offering strong evidence that they once contained standing bodies of water. By focusing our model to these sites, we can evaluate its ability to reproduce the formation of paleolakes.

3.2 Climate assumption and parameters exploration

The simulations presented here should be interpreted as an idealized reference case, in which precipitation and evaporation are prescribed as spatially uniform over the planetary surface. In this framework, the resulting steady states do not aim to reproduce a specific early-Mars climate scenario, but rather describe water distributions that are topographically reachable under globally distributed water input. The exploration of the parameter space allows to evaluate the sensitivity of the model to different climate conditions and initial states, and to identify the range of conditions that can lead to the formation of lakes and river networks. The homogeneous precipitation/evaporation pattern allows the identification, at the global scale, of water flow pathways and the locations of possible lakes.

This section defines the range of parameters explored in this conceptual application, including the evaporation rate E and the GEL. The evaporation rate E can be estimated using the following bulk aerodynamic formula:

$$E = \rho_{air} C_d v_{wind} [q_{sat}(T_{surf}) - q_{air}] \quad (9)$$

where ρ_{air} (kg m^{-3}) and v_{wind} (ms^{-1}) are respectively the volumetric mass of air and the wind velocity, C_d is the aerodynamic coefficient (unitless), $q_{sat}(T_{surf})$ is the water vapor mass mixing ratio at saturation at the surface which depends on the surface temperature T_{surf} , and q_{air} is the mixing ratio in the atmospheric layer. Assuming $C_d = 2.5 \times 10^{-3}$, $\rho_{air} = 0.02 \text{ kg m}^{-3}$, $q_{sat} = 0.01 \text{ kg kg}^{-1}$, neglecting q_{air} and by varying the wind velocity v_{wind} between 1 and 10 ms^{-1} (Wordsworth et al., 2015; Turbet et al., 2017), the evaporation rate E ranges from approximately 0.01 to 1 m yr^{-1} . This conceptual study proposes to test three evaporation rates: 0.01, 0.1 and 1 m yr^{-1} . Additionally, to test the robustness of this model, a non-realistic evaporation rate of 10 m yr^{-1} is also tested. Such value is much higher than the maximum evaporation rate observed on Earth, which is around 3 m yr^{-1} (Houston, 2006). This additional evaporation rate will allow to evaluate the model behaviour under extreme conditions and assess its ability to handle large volumes of water.

Moreover, several GEL values are investigated. Present-day Mars is estimated to have a GEL of approximately 34 m (Carr and Head, 2015), while the late Hesperian era is associated with a GEL of 64 m (Carr and Head, 2015). Other studies suggest higher values, such as 137 m (Villanueva et al., 2015), 550 m (Di Achille and Hynes, 2010), and even up to 1,500 m (Scheller et al., 2021) and 1,970 m (Jakosky and Hallis, 2024). To encompass this variability, four representative GEL values are selected for this conceptual study: 1 m, 10 m, 100 m, and 1,000 m.

To evaluate the sensitivity of the hydrological model to initial conditions, this GEL values are distributed in three distinct initial water distributions: a homogeneous distribution across the planet (Figure 4a), in the northern lowlands (75°N , 60°W , Figure 4b), and in the Hellas crater (40°N , 60°E , Figure 2c). These configurations allow us to assess the model response to varying initial states. Considering the tested evaporation rates, GEL values and initial states, a total of 48 simulations were performed to explore the parameter space.

3.3 Hydrological database

By using the MOLA topography map (Figure 2), the hydrological database was built on computing cluster (32 cores 2 AMD EPYC 7302 16-Core, 16GB of memory per core) in less than 2 days of computation time (41 hours equivalent to 1,312 CPU hours). The database contains 5,967,453 leaf depressions, 5,967,452 meta-depressions, i.e. a total of 11,934,905 depressions. The map of ID watershed and the watershed area A_i^w were used to build the Figure 3a. It shows the extent of the watersheds of leaf depressions near to the Gale crater (9,777 leaf depressions on this figure). This figure illustrates the high resolution of the database, higher than crater scale, which provides detailed information on the depressions and their associated watersheds. By looking at the craters on this map (circles contour plot, black lines), several depressions can be identified into them, including Gale crater, which is localized by the white star. The presence of depressions in the craters is due to local pits that are present in the craters.

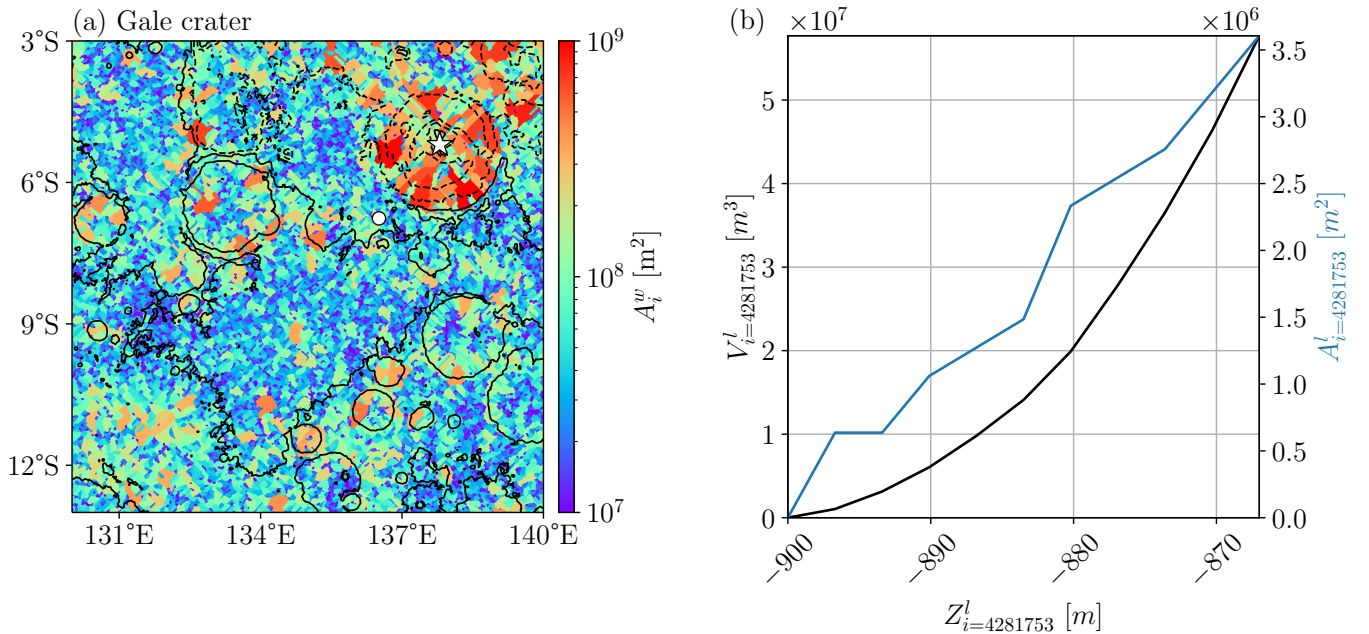


Figure 3. (a) 9,777 watersheds of leaf depressions are represented on the zoomed area of the Gale crater watershed (Figure 2d). Gale crater is localized by the white star. The color bar represents the watershed area A_i^w . (b) Example of pre-computed hydrological functions for a random depression ($i = 4281753$) localized near to the Gale watershed by the white point (a). Evolution of the lake volume V_i^l (black line) and the lake area A_i^l (blue curve) as functions of the lake elevation Z_i^l .

As mentioned in the section 2.2, the hydrological functions are pre-computed for each depression. The hydrological functions of a random depression ($i = 4281753$, white point in the map figure 3a) which is close to the Gale crater, are shown in Figure 3b. The pre-computed lake volume V_i^l and lake area A_i^l are plotted as functions of the lake elevation Z_i^l . As expected, the lake volume monotonically increases with the lake elevation, while the lake area can have a flat or increasing trend. The lake area function can not strictly increase because the lake area can remain constant with the lake elevation when a lake is bordered by

vertical cliffs for instance. The hydrological functions provide insights into the behavior of the depressions and their associated lakes, enabling the model to accurately simulate the water redistribution process.

3.4 Simulations and validation

Simulations were conducted on a supercomputer (32 cores 2 AMD Genoa EPYC 9654, 4 GB of memory per core), achieving a computational speed of approximately 22,000 iterations per day of simulation. A total of 48 simulations were performed to test the model sensitivity to the initial state (Figure 4a-c), the amount of water present on the planet and the fixed evaporation rate (Figure 4). The simulations were run for a maximum of 100,000 iterations. As shown in equations 5 and 6, the precipitation rate is directly linked to the lake area. A constant precipitation rate (i.e. a constant P/E ratio) indicates that the lakes are stable and that the model has reached a steady state (Figure 4d-g).

The timescale to reach equilibrium (Figure 4d-g) in our model depends primarily on the evaporation rate (E), the adaptive time step Δt and, to a lesser extent, on the Global Equivalent Layer (GEL) of water. The timescale varies linearly with the evaporation rate, as this parameter controls the rate of water transfer between depressions. Regarding the GEL , the timescale generally increases with GEL because a larger GEL implies that more water must be redistributed before equilibrium is reached. However, a high GEL also corresponds to a larger cumulative lake area, which increases the evaporated volume and thereby accelerates the redistribution of water. This explains why GEL has a secondary effect on the timescale to reach equilibrium. In our simulations, the timescale ranges from approximately 200 years for a GEL of 1 m and an evaporation rate of 1 m/yr, to over 100,000 years for a GEL of 1000 m and an evaporation rate of 0.01 m/yr. These timescales are consistent with geological constraints on valley network formation on early Mars, which suggest that they could have persisted for 10^5 to 10^7 years (Hoke et al., 2011).

The results also demonstrate that the model is not sensitive here to the initial state, as all simulations converge to the same P/E ratio for a fixed GEL . The Figure 4d-g illustrates, for homogeneous precipitation, that the final water distribution on the planet depend only on GEL value, s demonstrated in Appendix B. For a fixed GEL and homogeneous precipitation, the simulations confirm that the model is able of redistributing water across the planet and converging to a unique steady state. As expected, with this homogeneous climatic pattern, the converged P/E ratio depends only on the total lake surface area which is directly related to the GEL . It is also observed that the higher the GEL , the higher the final P/E ratio, as the water surface has a larger exchange area with the atmosphere. The precipitation pattern also controls the final water distribution and the resulting P/E ratio, as shown by simulations with a latitudinally varying precipitation pattern (Appendix C).

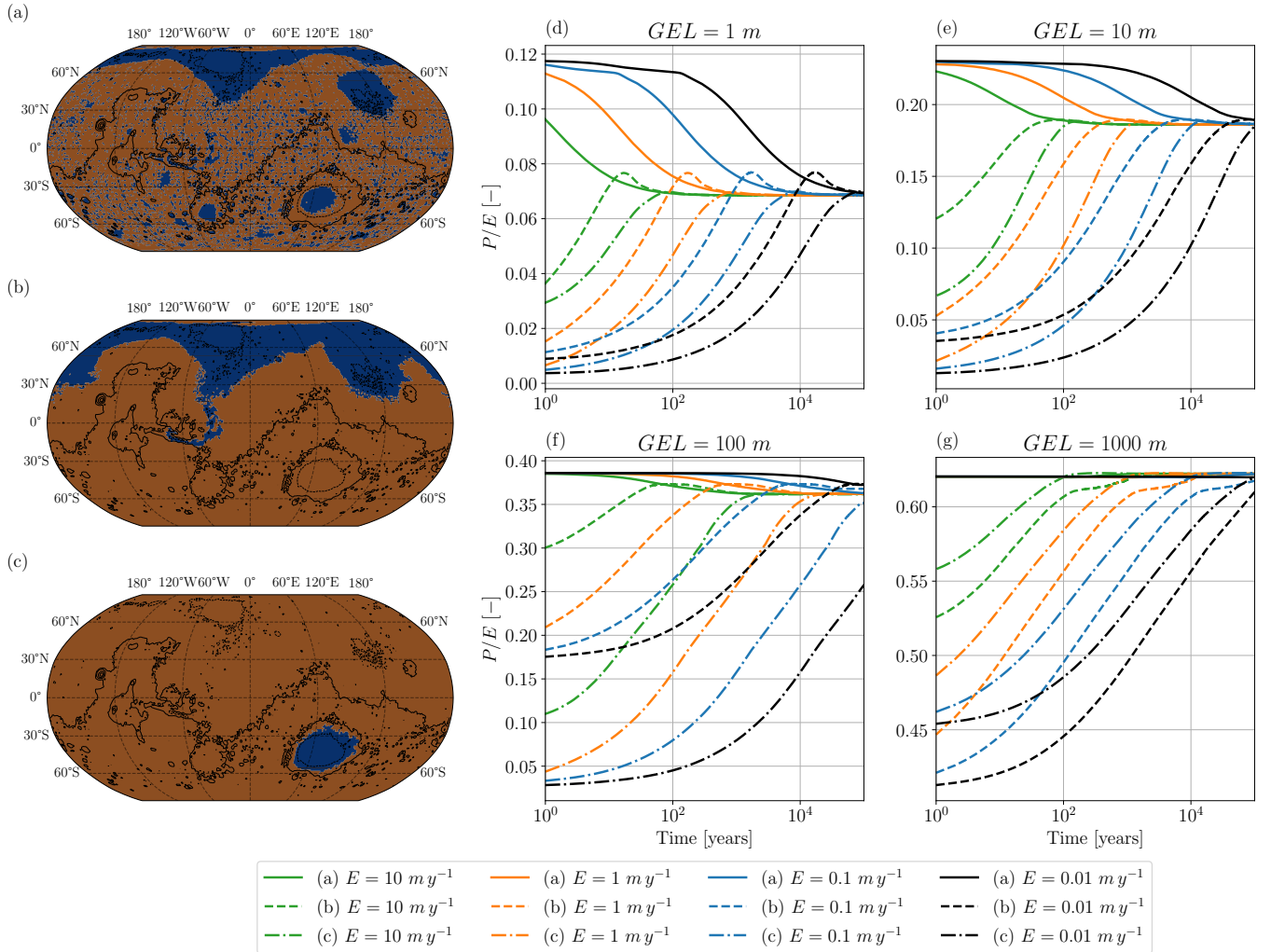


Figure 4. The three maps represent the initial states tested for a $GEL = 100$ m. The water is either distributed homogeneously (a), in the northern lowlands (b), or in the Hellas crater (c). The blue areas show the location of water reservoirs. The plots show the evolution of the P/E ratio over time for different GEL : 1 m (d), 10 m (e), 100 m (f), and 1,000 m (g). Solid lines, dashed lines, and dotted-dashed lines represent simulations with homogeneous water distribution (a), distribution in the northern lowlands (b), and in the Hellas crater (c), respectively. Green, orange, blue, and black lines represent simulations with fixed evaporation rates of 10, 1, 0.1, and 0.01 $m y^{-1}$, respectively.

3.4.1 Water distribution analysis

Figure 4 demonstrates that a unique steady state is reached for each GEL value, regardless of the initial water distribution or the evaporation rate. In this section, we analyze the resulting global water distribution for the four GEL scenarios. Figure 5 presents the steady-state distribution of water reservoirs, shown as sky-blue histograms. The left column displays the distribution as a function of latitude (1° bins), and the right column shows the distribution as a function of longitude. The cumulative relative

water volume (solid black line) is compared to a conceptual homogeneous distribution of water (dashed black line) from the north to the south-pole for the left column and from the west to the east for the right column. The extent of main reservoirs in the northern lowlands (Arcadia, Acidalia, Utopia, Isidis and Vastitas Borealis) and the southern basins (Solis, Hellas and Argyre) are represented by the vertical colored dashed lines and are localized on the water depth map (Figure 6a).

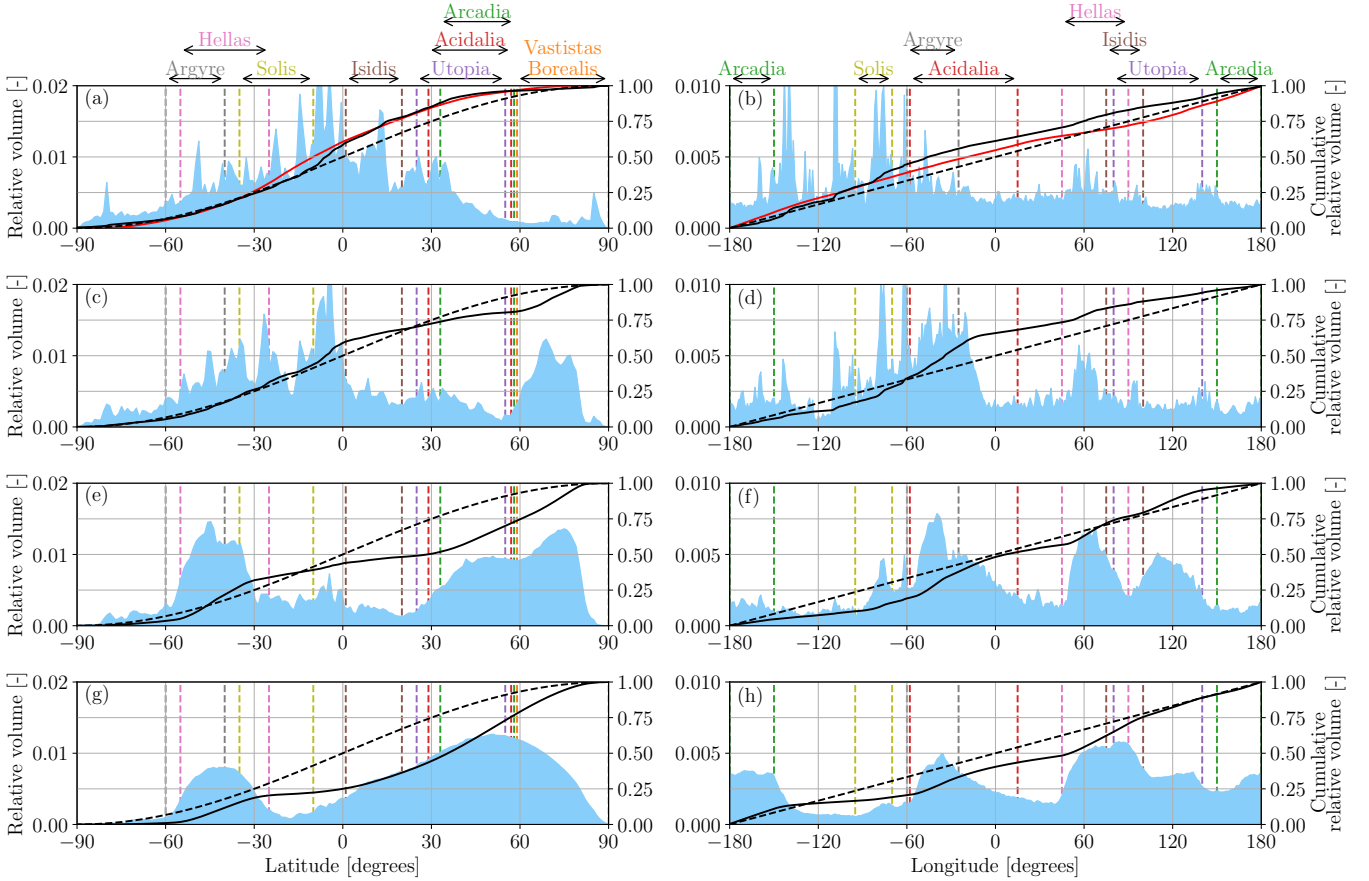


Figure 5. Distribution of water reservoirs at steady state for each GEL: 1 m (a, b), 10 m (c, d), 100 m (e, f), 1000 m (g, h). The blue areas represent the proportion of water relative to the total water volume (left y-axis) per degree of latitude (left column) and longitude (right column). The solid black lines show the cumulative relative water volume (right y-axis). The dashed black lines represent the cumulative relative water volume for a conceptual homogeneous distribution of water. The red curves on panels (a) and (b) represent the cumulative distribution of crater density (right y-axis) from Robbins and Hynek (2012).

For the simulation with the lowest GEL value (1 m, Figure 5a-b), the water is distributed relatively uniformly across the planet, with no significant regional accumulation (Appendix D1). According to latitude, the cumulative relative water volume (solid black line) closely follows the homogeneous distribution (dashed black line). However, there is a lack of stored volume between 40°N and 60°N, which is subsequently compensated by a larger storage between 0° and 15°S. This suggests that the region between 40°N and 60°N has fewer opportunities for retaining water, likely because it consists of relatively young,

less-cratered terrains with limited storage capacity as shown by the cumulative distribution of crater density (red curve, right y-axis, Figure 5a) from Robbins and Hynek (2012). As a result, water precipitating in this latitude band tends to flow toward the northern lowlands. Additionally, because the model applies spatially homogeneous precipitation, the northern lowlands progressively lose water to supply downstream regions. In particular, the area between 0° and 15°S – characterized by older, heavily cratered terrain – acts as a more efficient water sink, capable of retaining substantial volumes. These two processes together explain the observed deficit at mid-northern latitudes and the accumulation at southern equatorial latitudes. In terms of longitude, the distribution appears relatively uniform, with a slight concentration between 60°E and 120°E . This concentration can be explained by water convergence from the north to the south due to the steep slopes imposed by the Tharsis dome. For this amount of water, the distribution is relatively homogeneous across the planet, showing little concentration or/and overflow of water. It can be concluded that this quantity allows for minimal overflow on a planetary scale.

The simulation with a GEL of 10 m (Figure 5c-d) emerges distinct peaks in the distribution of water. In terms of latitude, a concentration appears between 60°N and 90°N , corresponding to the Northern Lowlands. In comparison to the GEL of 1 m, the distribution of water is mainly changed in the Northern Hemisphere, where the water is concentrated in the Northern lowlands (Appendix D2). This concentration is due to an overflow of water from the areas between 60°N and 0° to the Northern lowlands. The cumulative relative volume curve is significantly different from the homogeneous distribution in the Northern Hemisphere. Approximately 20% of the total water volume is stored in the Northern Lowlands, while the Southern Hemisphere remains close to the homogeneous distribution, like the case with a GEL of 1 m. The distribution in the Southern Hemisphere is relatively uniform, with a slight increase between 0° and 15°S . This indicates that the model is able to store this amount of water in the Southern Hemisphere and the area between 0° and 60°N is not favorable for water storage. Longitudinally, the distribution is also pronounced, with peaks at 0° and 120°W , corresponding to Acidalia Planitia, and at 60° and 120°W , corresponding to the Hellas Basin. The cumulative relative volume curve is significantly different from the homogeneous distribution, mainly because of the water accumulation in the north of Acidalia Planitia and in the Hellas basin.

For a GEL of 100 m (Figure 5e-f), the distribution changes significantly. The Northern Ocean expands considerably between 30°N and 90°N , accounting for approximately 50% of the total water volume. Arcadia Planitia, Acidalia Planitia and Utopia Planitia are the main flowed areas which contribute to the extension of the Northern Ocean. A significant amount of water is also stored in the Hellas and Argyre Basins, accounting for approximately 20% of the total water volume on the planet, which corresponds in quantity to the water stored between 30°N and 30°S . The distribution according to longitude shows that the water in the Northern lowlands is mainly concentrated in Acidalia Planitia and Utopia Planitia, while Hellas, Argyre and Solis Basins are the main flowed areas in the Southern Hemisphere. Figure 6 illustrates spatially the main water reservoirs at steady state. As mentioned previously, the water depth map shows that the water is mainly stored in the northern lowlands and crater impacts, but it can also be stored in low slope areas with a natural barrier allowing to block the water flow. The zoomed maps show that all craters are filled with water due to homogeneous precipitation. Moreover, in addition to the craters, there are many local areas with thin water depth. In the zoomed maps, the valley network can also be distinguished, mainly the Nirgal Vallis (Figure 6b) and the valley network that feeds the Gale crater (Figure 6d).

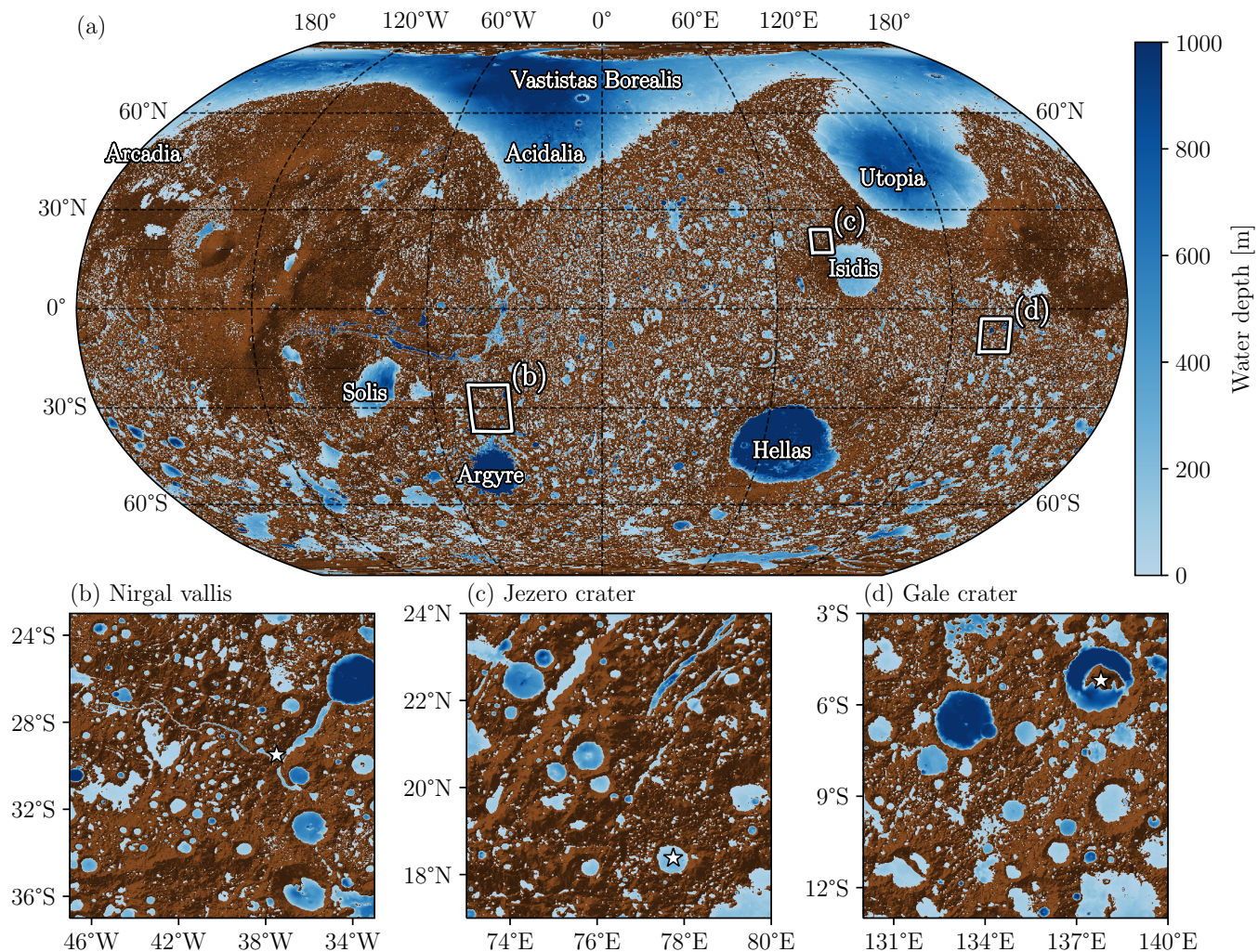


Figure 6. Distribution of water reservoirs (blue areas) at steady state with a GEL equal to 100 m. The color bar represents the water depth. The brown shaded areas represent the areas where the water cannot be accumulated. The white squares are zoomed areas on Nirgal Vallis' watershed (b), Jezero' watershed (c) and Gale' watershed (d). The white stars localized the Nirgal Vallis outlet (b), Jezero crater (c) and Gale crater (d).

The simulation with the highest GEL value (1,000 m, Figure 5g-h) shows a significant increase in the volume of water stored in the Northern Ocean, which accounts for approximately 75% of the total water volume (Appendix D3). The Hellas Basin remains a significant reservoir, accounting for approximately 20% of the total water volume. The distribution according to latitude shows that the water is mainly concentrated in the Northern Hemisphere and in the Hellas Basin. The distribution according to longitude shows that the water is mainly concentrated in Acidalia Planitia, Utopia Planitia and Arcadia Planitia. The cumulative relative volume curve is significantly different from the homogeneous distribution, mainly because of the water accumulation in the Northern lowlands and in Hellas basin.

This analysis shows that between a GEL of 1 m and 10 m, a formation of a northern ocean begins to emerge. Overall, regions with limited water retention are found in the sparsely cratered zone between 30°N and 60°N and in the Tharsis dome area, where steep slopes promote rapid overflow and hinder accumulation. As the GEL value increases, the proportion of water stored in the Northern Hemisphere significantly rises. Similarly, an evolution in the water distribution is observed from west to east with increasing GEL values. Higher GEL values lead to a greater proportion of water being concentrated in the eastern part of the planet (0°E to 180°E).

3.4.2 Water outflow analysis

At steady state, although water distribution across the planet depends on the GEL, the water outflow rate is primarily controlled by the precipitation rate P , which depends on the evaporation rate E and the GEL (i.e. oceans/lakes area A_i), and whether the depression is filled to allow the overflow. The comparison between Figure 7 and the figures in Appendix D (Figures D2, D4 and D6) shows that the water outflow rate increases with the GEL, as the lake area increases with the GEL.

The water outflow map (Figure 7a) shows the water flow accumulation at steady state for a GEL of 100 m and an evaporation rate of 1 m yr^{-1} . The water overflow Q_i^{out} is displayed on the watershed area for each depression where the lake overflows. This figure allows to keep a continuity between depressions and easily visualize the water flow pathways. In case there is no overflow, the lake areas are displayed by a transparent sky blue area. The white shaded areas represent the watershed area where there is no overflow. This result highlights four main valley networks that drain the water from the highlands to the Northern Ocean. Three of them finish their path in the part of the ocean corresponding to Acidalia Planitia, while the fourth one drains the water to the ocean corresponding to Arcadia Planitia. These valley networks are mainly located near the Tharsis dome, which is a highland area with steep slopes and no water reservoir to retain the water, that facilitates the water flow.

The highest simulated water outflow is observed near Marte Vallis (Amazonis Planitia). The outlet coordinates are located at 174°W, 42°N, with a discharge of approximately $66,034 \text{ m}^3 \text{ s}^{-1}$. To the east of the outlet, the river drains Elysium Planitia, particularly the region south of Elysium Mons. To the west of the outlet, the river collects water from the entire Olympus Mons area and the western and southern regions of the Tharsis Montes. The river with the second-highest flow is located at the junction between Simud Vallis and Lobo Vallis (coordinates 36°W, 35°N). This river drains the eastern part of the Tharsis dome and the Valles Marineris region. The flow rate is approximately $29,411 \text{ m}^3 \text{ s}^{-1}$. The outlet of the third productive river is located near the previous one, at coordinates 30°W, 30°N, corresponding to Ares Vallis. This river drains the elevated and cratered region of Noachis Terra (between 30°W and 30°E) and the area situated between Valles Marineris and Argyre Planitia. The flow rate is approximately $12,362 \text{ m}^3 \text{ s}^{-1}$. The last major productive river highlighted in this simulation drains the northern region of Tharsis. Originating in the Tharsis region, specifically near Ascreaus Mons, it flows northward, terminating at coordinates 65°W, 57°N. The flow rate of this river is approximately $9,176 \text{ m}^3 \text{ s}^{-1}$. The discharge rates in this simulation are comparable to those observed in some of Earth's largest rivers. For instance, the Amazon River, the largest river on Earth by discharge, has an average flow rate of approximately $209,000 \text{ m}^3 \text{ s}^{-1}$ (Dai and Trenberth, 2002), which is significantly higher than the simulated rivers. The Congo River, with an average discharge of around $41,000 \text{ m}^3 \text{ s}^{-1}$, is closer to the simulated outflows, particularly the Marte Vallis outlet. Similarly, the Ganges-Brahmaputra River system, with an average discharge of

approximately $35,000 \text{ m}^3 \text{ s}^{-1}$, and the Orinoco River, with about $32,000 \text{ m}^3 \text{ s}^{-1}$, also fall within the range of the simulated river discharges. Additionally, the Saint Lawrence River, with an average discharge of approximately $10,000 \text{ m}^3 \text{ s}^{-1}$, provides an example of a terrestrial river with a flow rate comparable to the last mentioned simulated river. These comparisons highlight that the modeled hydrological system could produce flow rates similar to some of Earth's major river systems.

Nirgal Vallis (Figure 7b) is part of the upstream section of the river system that ultimately flows into Ares Vallis, with a simulated discharge of $3,700 \text{ m}^3 \text{ s}^{-1}$ at his outlet (white star). However, when compared to the observed river network map (Hynek et al., 2010) shown in Figure 2b, the simulated and observed river pathways do not spatially align. The simulated river drains a significantly larger area than what is observed, suggesting that the actual discharge of Nirgal Vallis may be lower than the modeled value in this simulation.

Jezero Crater (Figure 7c) is fed by two rivers converging from the north and northeast. The discharge of the northern river is $50.6 \text{ m}^3 \text{ s}^{-1}$, while the northeastern river has a discharge of $45.8 \text{ m}^3 \text{ s}^{-1}$. The volumes contributed by the two rivers are relatively similar. Closed lakes that do not overflow are also observed upstream of the Jezero system. These closed systems could occasionally act as reservoirs contributing to the inflow of Jezero Crater.

In the case of Gale Crater (Figure 7d), two river systems also converge, but with significantly different discharges: $79.5 \text{ m}^3 \text{ s}^{-1}$ for the northern river and $120.2 \text{ m}^3 \text{ s}^{-1}$ for the southern river. Unlike Jezero Crater, the confluence occurs well before the water reaches Gale Crater. Additionally, other smaller streams contribute between the confluence and the crater. The total discharge of the river entering Gale Crater is $244.1 \text{ m}^3 \text{ s}^{-1}$, highlighting the significant contribution of upstream flows to the crater hydrological system.

The proposed representation allows for the study of water exchanges between the watersheds of depressions. We propose to go further in the spatial representation of the results by adding a post-processing step to the hydrological model outputs to identify rivers and the exact pathways of water flow between lakes. The post-processing results presented in Section 2.4 are shown in Figures 7e-g. This representation allows to identify the exact paths taken by water and to delineate watersheds. While lakes are well represented spatially, the widths of the rivers displayed in this figure are not to scale but rather serve as a mapping of their locations. This post-processing will facilitate the comparison with observed valley networks on Mars and provide a better understanding of water exchanges between reservoirs.

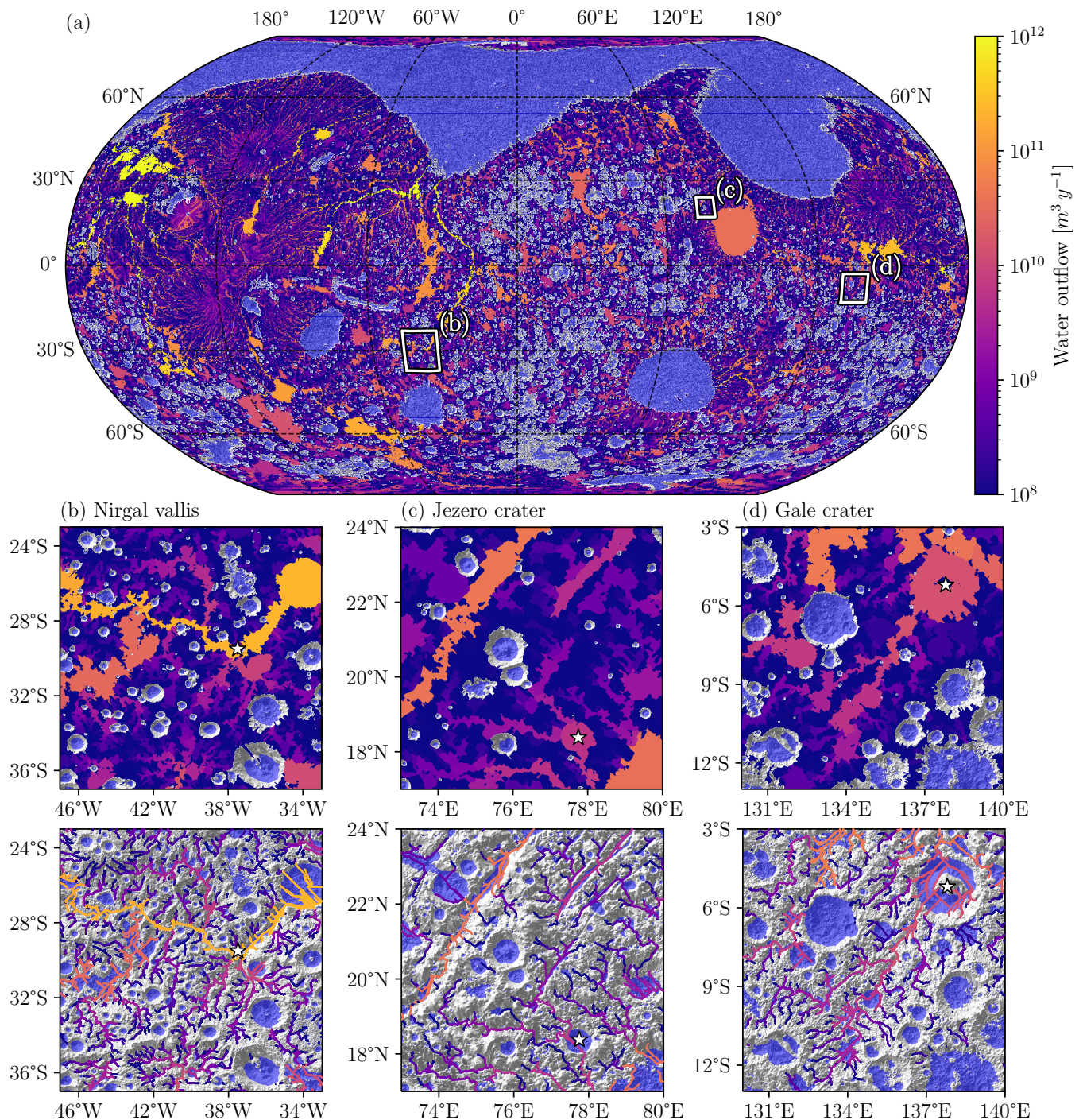


Figure 7. Water overflow at steady state with a $GEL = 100$ m. The color bar represents the water flow accumulation. The areas where there is no outflow are symbolized by white shaded areas and sky blue areas represent the watershed and lake/ocean areas. The first line of zoomed plots shows the raw output data of the hydrological model which represents the water overflow associated to the watershed area. The second line of zoomed plots shows the water overflow associated to the valley network, after post-processing explained in section 2.4.

4 Discussions and perspectives

4.1 Topography dependence

The main limitation is the model dependence on the topography map which is a crucial input for the construction of the hydrological database, as it defines the watershed of depressions and their spillover point. The resolution of the topography map can significantly impact the model ability to accurately represent the hydrological features of the planet. We tested the model with the MOLA topography map degraded to 1 px/degree. The model was run with a GEL of 100 m and an evaporation rate of 1 m yr^{-1} . The model is compared with results using the high resolution topography map (128 px/degree). The Figures 8b-c show the water distribution according to longitude and latitude. As Figure 5, the histogram shows the relative water volume as a function of latitude/longitude degree and the solid line shows the cumulative relative water volume. While the distributions of water reservoirs are relatively similar according to longitude, the distributions according to latitude are significantly different, notably in the Northern Hemisphere. The high resolution model transfers more water to the Northern lowlands, while the low resolution model shows a more uniform distribution of water across the area between 90°N and 0° . This difference can be explained by the fact that the smoothing of the topography map can increase the elevation of the spillover point and consequently increase the storage capacity of the depressions.

The same work was done with a pre-True Polar Wander (TPW) topography map (Bouley et al., 2016) (Figure 8a). This topography map contains significantly less depressions (craters) than the current MOLA topographic map and the Tharsis region is not represented. As expected, the pre-TPW model shows a significant difference in the distribution of water reservoirs compared to the model based on MOLA topography. If the pre-TPW topography accumulates less water in the Northern Hemisphere, around 45% of the total water volume is stored in lower latitudes, between -15° and 60°N , placing one of the main reservoirs closest to the equator than in the current topography (Figure 8c). In the Southern Hemisphere, the water is mainly concentrated between 0° and 45° in the Hellas and Argyre basins.

According to the longitude (Figure 8b), we can observe an absence of water accumulation in the area between 30°W and 30°E , characterized by the flat curve of the cumulative relative water volume. In the Southern Hemisphere, this area corresponds to the Noachian highlands, which are preserved in the MOLA topography. The previous simulations with the MOLA topography show that these areas are favorable for water storage, as they are heavily cratered and contain many depressions. The absence of water accumulation in the area between 30°W and 30°E in the pre-TPW topography, and the reduced water storage in the northern lowlands compared to MOLA (whether high or low resolution), suggests that the differences arise from fundamental topographic changes rather than resolution effects alone. The degraded MOLA topography (1 px/degree) maintains water pooling in the -30° to 30°E longitude band and in the northern lowlands, demonstrating that coarse resolution alone does not eliminate these features. The pre-TPW topography, by contrast, shows a qualitatively different hydrological configuration: the vast interconnected northern ocean present in both MOLA versions is largely absent in the pre-TPW case. This indicates that the True Polar Wander rotation, crater relaxation, and volcanic infilling that occurred between the pre-TPW and present-day have substantially modified the topographic depressions. This result suggests that using the current topography

map brings some challenges to understand early Mars. However, models of water surface flow on early Mars are limited by our ability to reconstruct the ancient surface topography.

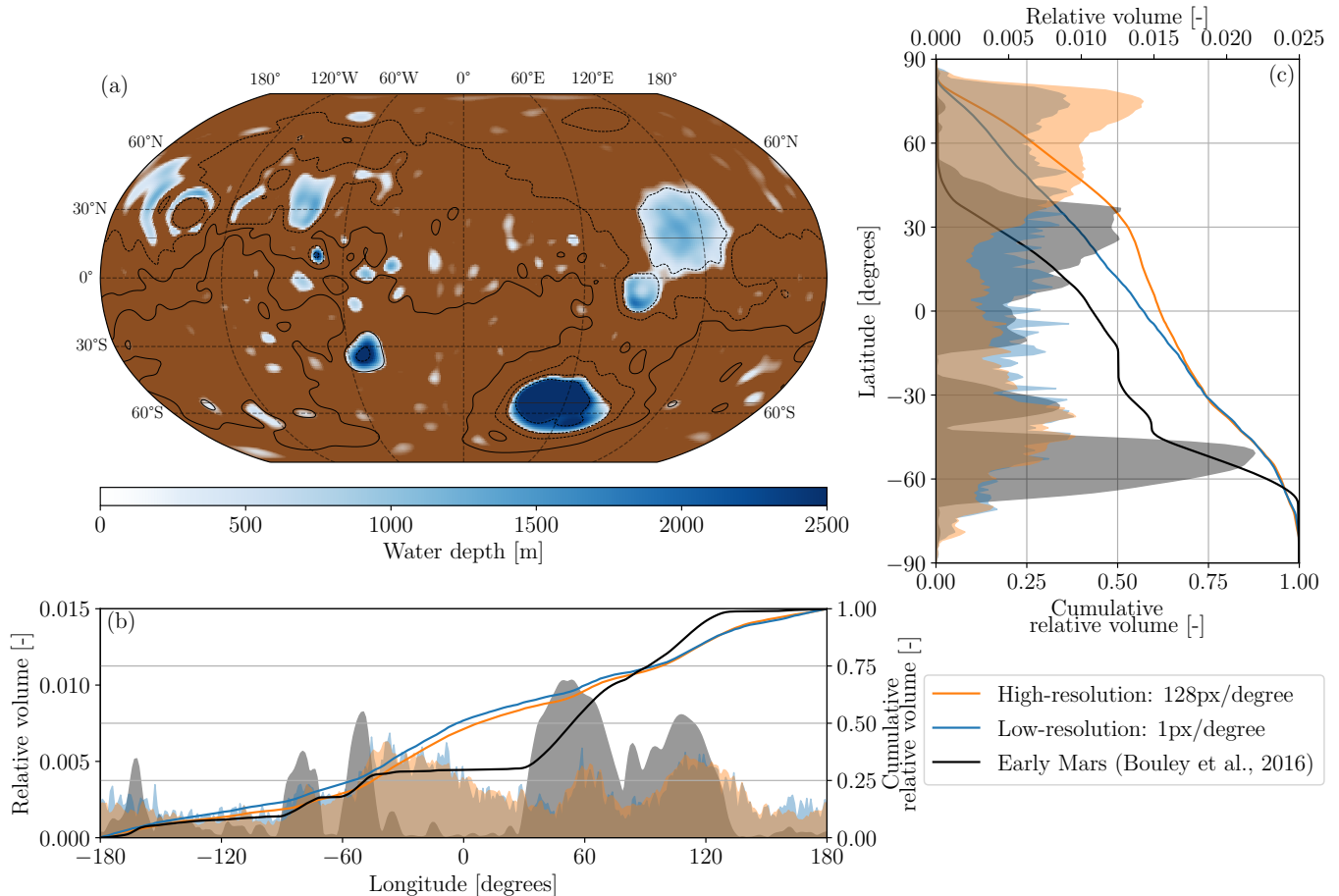


Figure 8. (a) Distribution of water reservoirs (blue areas) on pre-TPW topography (Bouley et al., 2016) at steady state with a GEL equal to 100 m. The color bar represents the water depth. The brown areas represent the areas where the water cannot be accumulated. (b-c) The solid black lines show the cumulative relative water volume per degree of longitude (b) and latitude (c). Three models are compared: the current MOLA topography (128 px/degree, orange line), the degraded MOLA topography (1 px/degree, blue line) and the pre-TPW topography (1 px/degree, black line).

To fully leverage the potential of such a hydrological model, it would be essential to use a high-resolution topography map that accurately represents the surface of early Mars. This would involve reconstructing the topography by removing the effects of the True Polar Wander (TPW) event (Bouley et al., 2016; Phillips et al., 2001). Additionally, the exclusion of younger craters that formed after the Noachian period would be crucial, as their presence introduces additional reservoirs that were not part of the ancient Martian landscape (Morgan, 2024; Liu et al., 2024). This reconstructed map would provide a more accurate representation of the ancient Martian surface, enabling better simulations of early hydrological processes and

facilitating comparisons with geological and geomorphological observations. An additional improvement for reconstructed ancient topography maps would be to artificially "recraterize" younger terrains. This could be achieved by statistically adding impact craters using a realistic size-frequency distribution, consistent with the expected crater population for the Noachian or Hesperian epochs. Such an approach would help restore the hydrological storage capacity and drainage patterns that would have existed prior to resurfacing events, thereby improving the fidelity of hydrological simulations on early Mars.

4.2 Groundwater processes

In these results, we assume no infiltration ($\beta = 1$) and neglect subsurface flows. However, incorporating infiltration (Shadab et al., 2025) and groundwater flow processes could significantly improve the model ability to simulate the Martian hydrological cycle, offering valuable insights into the interactions between surface water and the Martian subsurface. The process of infiltration and groundwater flow can significantly influence the distribution and retention of surface water on the planet. By adding these processes to our hydrological model, we would expect a redistribution of surface water driven by subsurface flow, with contrasting effects depending on topographic setting. In particular, surface water retention would likely be overestimated in high-elevation depressions, where infiltration would induce lake volume losses through recharge of the subsurface. Conversely, surface water retention would likely be underestimated in low-elevation depressions, which would act as groundwater convergence zones, receiving additional water through subsurface flow and thus sustaining larger or more persistent surface water bodies.

This implementation would allow the simulation of processes such as aquifer recharge, subsurface flow pathways and groundwater discharge/sapping. Developing a global groundwater flow model, inspired by terrestrial hydrological frameworks (Fan and Miguez-Macho, 2011; Verkaik et al., 2024) and previous Martian studies (Luo and Howard, 2008; Horvath and Andrews-Hanna, 2021, 2017; Harrison and Grimm, 2005; Andrews-Hanna et al., 2010; Hiatt et al., 2024), could further enhance the integration of surface and subsurface hydrological processes to compare, for instance, the model outputs with the U- and V-shaped valley networks profiles (Williams and Phillips, 2001) which result from the groundwater sapping and surface runoff, respectively.

4.3 Climate coupling

In this conceptual study, the precipitation rate P , which depends on the evaporation rate E and the lake surface area, is considered homogeneous. This simplification allows the model to simulate a steady state, where the hydrological system reaches equilibrium. The steady-state results can be analyzed using metrics such as the X ratio (Matsubara et al., 2013, 2011) or the Aridity Index (AI) (Stucky de Quay et al., 2020). The X ratio, defined as the ratio of evaporated water to precipitated water, provides a quantitative measure of the hydrological balance in a region. Similarly, the Aridity Index (AI), calculated as the ratio of lake area to the total watershed area, offers insights into the spatial distribution of water and the relative humidity of different regions. These metrics also enable comparisons with previous works.

By coupling the hydrological model with a GCM, it becomes possible to explore the interactions between atmospheric circulation, spatial and temporal precipitation/evaporation variations. This coupling would provide a more comprehensive

understanding of Mars' water cycle, enabling the study of dynamic processes such as the formation and disappearance of waterbodies according to the seasons. Additionally, the model could be extended to study transient hydrological states, such as the formation of large valleys in the Martian highlands caused by catastrophic paleolake overflows (Irwin III et al., 2004). These events, driven by sudden breaches in crater rims or other topographic barriers, could have significantly reshaped the Martian surface. By simulating such transient events, the model could help identify the conditions under which these features formed, linking them to specific climatic and hydrological scenarios.

The next goal of our work is to integrate this hydrological model into the Planetary Evolution Model (PEM) (Forget et al., 2024; Clément et al., 2024), a new modelling framework based on an asynchronous coupling with a GCM. The PEM can simulate long-term climate dynamics which allow us to study the impact of orbital-scale climate variations on the water cycle. In particular, we could investigate long-term accumulation/depletion of liquid water in lakes, including their cycle due to temperature and pressure changes, runoff after precipitation, the transport of water by rivers, the diffusion of water into the deep subsurface, etc. Moreover, the PEM can be used to set initial states for other simulations by determining steady-state realistic distribution of water for given orbital parameters.

4.4 Comparison tool

A quantitative comparison between simulated water distributions and observed geomorphological features on Mars (Figure 2) would strengthen the validation of our model. However, such a comparison is constrained by two key limitations in the current work. First, the assumption of spatially uniform precipitation is a strong constraint that may not reflect the realistic precipitation patterns predicted by Global Climate Models for early Mars (Turbet and Forget, 2021; Wordsworth et al., 2015, 2013). Second, the use of present-day MOLA topography, rather than a reconstructed ancient surface, introduces systematic biases in the spatial distribution of depressions and their connectivity. Despite these limitations, our results provide useful insights: the 100 m GEL simulation broadly reproduces the northern ocean extent between the Arabia and Deuteronilus shoreline levels, and the model successfully identifies the major topographic basins (Hellas, Argyre, northern lowlands) as primary water repositories.

By coupling this model with a GCM, we will be able to compare simulation results with geological and geomorphological observations. For instance, we can compare the simulations with existing databases on open- and closed-basin lakes (Goudge et al., 2016; Fassett and Head, 2008), identified deltas (Di Achille and Hynek, 2010), potential shorelines (Sholes et al., 2021) and valley networks (Hynek et al., 2010). Additionally, the results can be compared with detected hydrated minerals (Bibring et al., 2006) and stratified sedimentary deposits (Malin and Edgett, 2000; Horvath and Andrews-Hanna, 2017), using lake levels and river discharges to estimate sedimentary deposits. Finally, the simulated river discharges can be compared with estimates of Martian fluvial discharges (Mangold et al., 2013), thereby validating and refining hypotheses on Mars' hydrological and climate evolution.

5 Conclusions

We developed a global high-resolution surface hydrological model that explicitly exploits a pre-computed hierarchical depression graph and lake volume–area–elevation functions to simulate the redistribution of liquid water over planetary topography. Applied here to present-day and reconstructed Martian topographies, the model efficiently identifies storage areas (lakes, seas, putative oceans), their spillovers, and the integrated drainage pathways. The hydrological database (nearly 12 million depressions) and lookup strategy enable rapid iterative equilibration under simple forcing, providing a scalable framework for future climate coupling. Systematic exploration of Global Equivalent Layer (GEL) and evaporation configurations shows: (i) convergence to a unique steady-state water distribution that depends only on total water volume (GEL) and topographic structure under homogeneous forcing; (ii) the emergence of a contiguous northern ocean between GEL values of order 1–10 m; (iii) a progressive concentration of water storage in the northern lowlands, Hellas, and Argyre with increasing GEL (up to 75 % of total volume in the northern basin at 1000 m GEL); (iv) organization of four main trunk drainage systems funneling highland runoff toward Acidalia, Arcadia and adjacent sectors, broadly consistent with large-scale slope controls. The model further reproduces local-scale reservoir connectivity for sites of interest (e.g. Jezero, Gale), offering quantitative estimates of inflow partitioning and discharge magnitudes. While the model can reproduce many observed features, limitations remain, particularly regarding the current topography used and the absence of subsurface flows. Future work will focus on integrating these processes and coupling the hydrological model with a Global Climate Model (GCM) to explore the interactions between Mars’ hydrology and climate. Additionally, the model robustness will be further tested by incorporating alternative topographic reconstructions. Overall, this work establishes a physically consistent yet computationally efficient foundation for simulating the large-scale organization of surface liquid reservoirs at planetary scale. It provides a bridge between geomorphological evidence and climate scenario testing, and a platform upon which progressively richer hydrological and climatic processes can be integrated to refine constraints on the planet’s aqueous and atmospheric evolution.

Code and data availability. MOLA topography map can be retrieved from the NASA Planetary Data System PDS (Smith et al., 1999). The current version of the model is available under the CeCILL licence. The exact version of the model used to produce the results used in this paper is archived on repository under <https://doi.org/10.5281/zenodo.17208793> (Gauvain, 2025), as are input data and scripts to run the model and produce the plots for all the simulations presented in this paper.

Appendix A: Algorithm comparison to compute lake elevation/area

The Pseudo-code 6.3 (FillDepressions) from Barnes et al. (2021) has been implemented into our hydrological model to compute lake areas and levels. This allows the comparison between the Interpolation of Pre-computed lake Functions (IPF) and the Fill–Spill–Merge (FSM) algorithm and illustrates the efficiency benefits of our approach. For this comparison, we recomputed the lake area and elevation for each active depression of the result' simulation at steady state for the 100 m GEL presented in Figure 6 of the manuscript. In this final state, there are 2,059,551 active depressions. We calculated the lake areas and elevations of these depressions using both the IPF and FSM algorithms.

The results show very good agreement between the two methods (Figure A1a), with a mean error of 1.44 pixels (using the largest cell size of the DEM, 423×423 , m at the equator) for the lake area. This discrepancy arises from the difference between the step function computed with FSM and the pre-computed function, which is based on a linear interpolation of the lake area (Figure A1c). Comparison of the lake elevations also shows good agreement (Figure A1b), as the functions are very similar (Figure A1c). The total CPU time required to process the 2,059,551 depressions is 1.88 hours for the FSM algorithm (recall that the DEM contains 1,061,683,200 pixels), compared with only 4.75 seconds for the IPF approach (Figure A1d).

This comparison clearly demonstrates that our method is significantly more efficient than directly computing lake levels with FSM, while still providing accurate estimates of lake areas and elevations. Additionally, we want to mention that the computation of lake area and elevation is performed at every time step of the simulation, which further emphasizes the importance of computational efficiency in our approach.

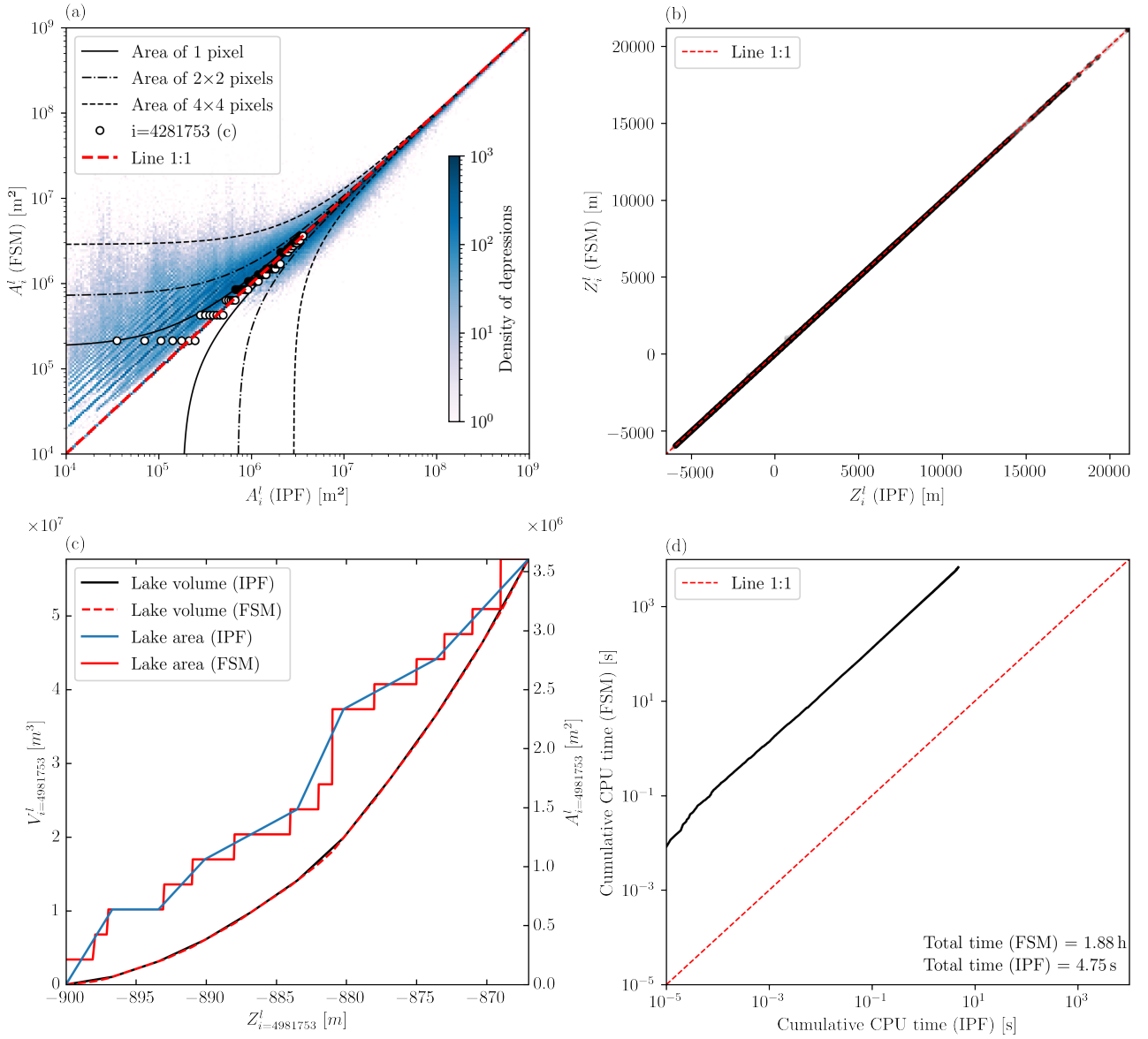


Figure A1. (a) Comparison of the lake area A_i^l computed using the interpolation of pre-computed lake functions (IPF) and the Fill-Spill-Merge (FSM) algorithm. The comparison is performed for all active depressions (2,059,551 depressions) shown in Figure 5 (100 m GEL simulation). The color bar indicates the density of depressions. The three black lines (solid, dashed, and dash-dotted) represent errors of 1 pixel (423×423 m), 4 pixels, and 16 pixels, respectively. The white dots indicate the comparison between the blue and red solid curves in panel (c) for depression $i = 4,281,753$. (b) Comparison of the lake elevation Z_i^l computed using the interpolation of pre-computed lake functions (IPF) and the Fill-Spill-Merge (FSM) algorithm. (c) Pre-computed hydrological functions (IPF) and functions computed with the Fill-Spill-Merge (FSM) algorithm for a single depression ($i = 4,281,753$) shown in Figure 3. (d) Comparison of computation times for the two algorithms. The total CPU time for the 2,059,551 depressions is 1.88 hours for the Fill-Spill-Merge algorithm, compared with 4.75 seconds for the interpolation of pre-computed functions (IPF).

Appendix B: Analytical demonstration

The presented model is designed to reach a steady state where the water volume, lake surface area, and lake elevation in each active depression remain constant. To demonstrate the model ability to reach this equilibrium, an analytical demonstration is proposed to show that the filling of the different lakes depends only on the total available water volume and not on the assumed precipitation or evaporation rates. We consider a global hydrological network without subsurface connections, filled with a total water volume V_{tot} (m^3) and subjected to an homogeneous precipitation P (ms^{-1}) and a potential evaporation E (ms^{-1}). There are N lakes, potentially connected (open lakes), within N watersheds of area A_i^w (m^2). For each lake, the volume V_i (m^3) is related to the lake area A_i (m^2) by the function $V_i = f_i(A_i)$. The maximum volume V_i^{max} and the maximum lake area A_i^{max} at overflow are known for open lakes. At equilibrium, for an isolated closed lake i , the evaporation from the lake compensates for the precipitation falling on its watershed area:

$$EA_i = PA_i^w \quad \Rightarrow \quad A_i = (P/E)A_i^w \quad (B1)$$

For a system of N open lakes connected by overflow pathways, there is always a closed lake n located downstream of the system. Then, for all n , the Equation B1 can be written as:

$$E \left(\sum_{i=1}^{N-1} A_i^{max} + A_n \right) = P \sum_{i=1}^N A_i^w \quad \Rightarrow \quad A_n = \left(\frac{P}{E} \right) \sum_{i=1}^N A_i^w - \sum_{i=1}^{N-1} A_i^{max} = g_n(P/E) \quad (B2)$$

where g is a linear function, since both $\sum_{i=1}^N A_i^w$ and $\sum_{i=1}^{N-1} A_i^{max}$ are constant. Thus, A_n depends only on P/E , ensuring a unique relationship. This analytical result demonstrates that, at equilibrium, the distribution of water among the lakes depends exclusively on P/E . It can be noted that numerical artifacts depending on discretization (e.g., "vertical" lake shores) can make non-strictly monotonic functions. According to the equation B2, the total water volume stored in the lakes is given by:

$$V_{tot} = \sum_{i=1}^N V_i = \sum_{i=1}^N f_i(A_i) = \sum_{i=1}^N f_i(g_i(P/E)) \quad (B3)$$

Since the functions g_i and f_i are strictly monotonic, V_{tot} depends only on P/E . It follows that for a given E and V_{tot} , there exists a unique corresponding value of P . This demonstration highlights the fundamental role of the GEL (i.e. V_{tot}) in shaping the steady-state hydrological configuration of the system.

Appendix C: Heterogeneous precipitation patterns

Sensitivity experiments with non-uniform precipitation patterns (Figure C1) were conducted to highlight the influence of the precipitation regime pattern. Three idealized precipitation patterns were tested: a homogeneous pattern (Figure C1a), a pattern concentrated around 20°N (Figure C1b), and a pattern concentrated around 20°S (Figure C1c). The results show that the equilibrium states are not unique for a given GEL when the precipitation pattern is non-uniform (Figure C1d). The final P/E ratio also varies significantly with the precipitation pattern. The water distribution at steady state is strongly influenced by the precipitation pattern (Figure C1e-f-g), with water accumulating in regions of enhanced precipitation and drying out in regions of reduced precipitation.

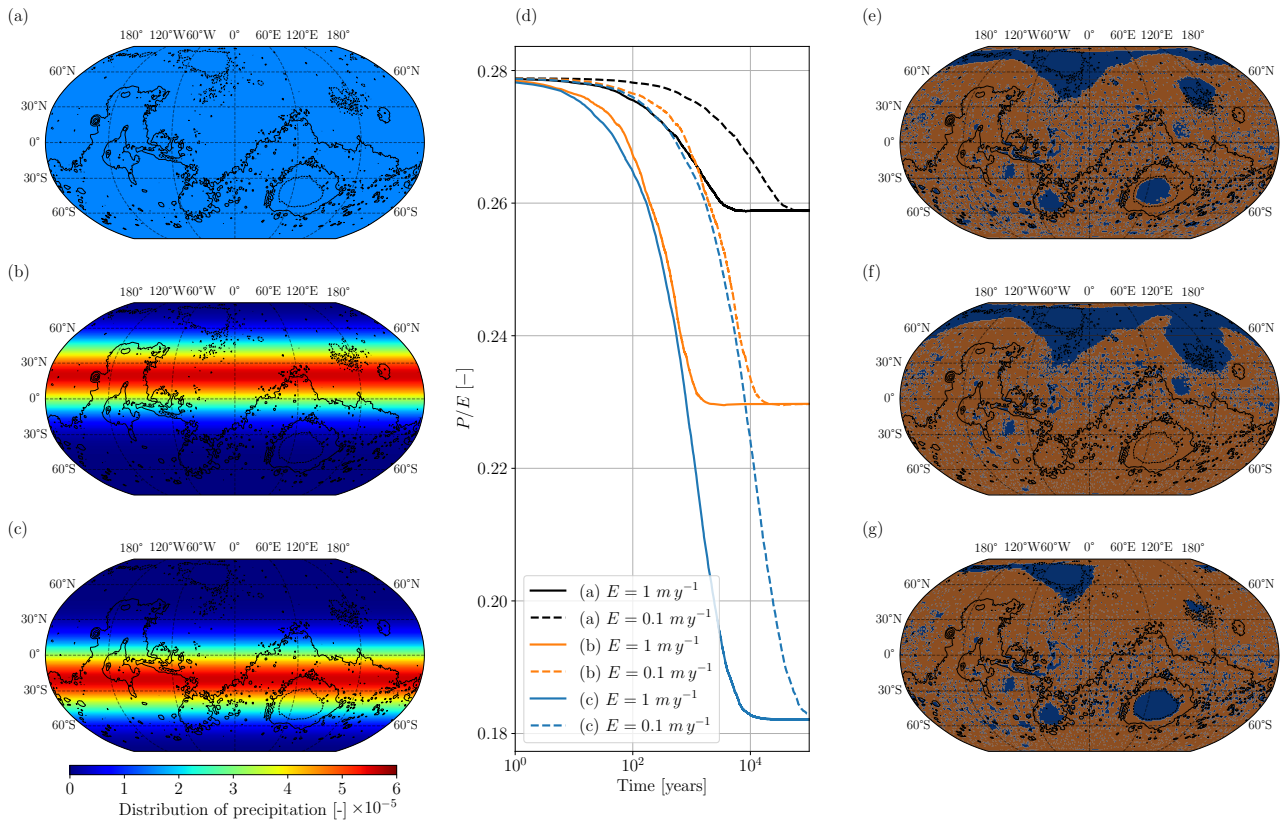


Figure C1. Simulations at steady state for a GEL = 100m with a varying precipitation pattern: (a) homogeneous precipitation pattern, (b) precipitation is concentrated around 20°N and (c) precipitation concentrated around 20°S . Simulations were performed with a degraded MOLA topography at 1 pixel per degree resolution. (d) Evolution of the ratio P/E for the three precipitation rate patterns and two homogeneous evaporation rate: 1 m/yr (solid curves) and 0.1 m/yr (dashed curves). Distribution of water reservoirs at steady state for the three precipitation patterns: (e) homogeneous precipitation pattern, (f) precipitation is concentrated around 20°N and (g) precipitation concentrated around 20°S .

Appendix D: Water distribution and water outflow

In this appendix, we present the water distribution and water outflow maps at steady state for different GEL values (1 m, 10 m and 1,000 m) with an evaporation rate of 1 m yr^{-1} . These results complement those presented in sections 3.4.1 and 3.4.2 for a GEL of 100 m. The colorbars are consistent to facilitate comparison between the different results.

D1 Global Equivalent Layer of 1 m

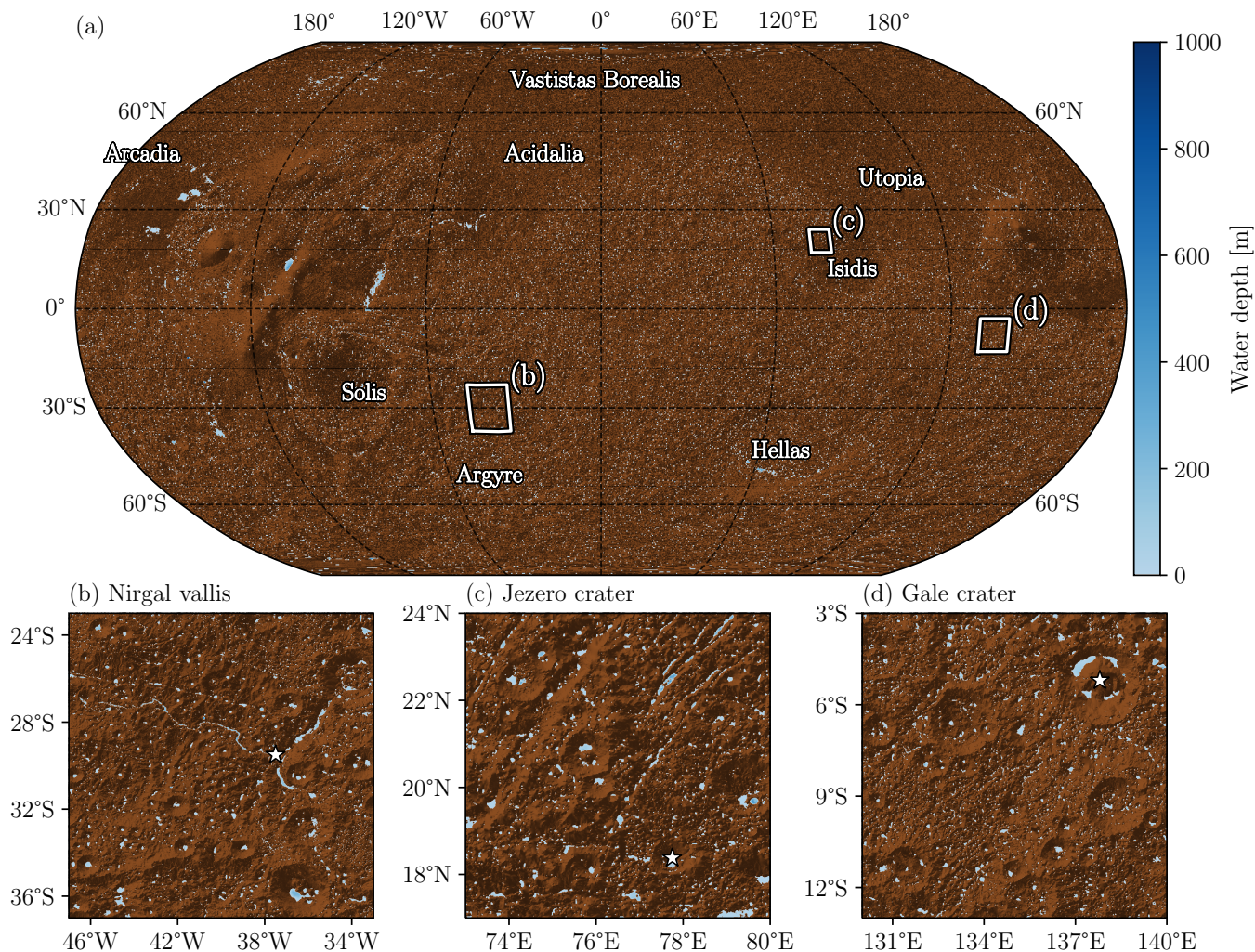


Figure D1. Distribution of water reservoirs (blue areas) at steady state with a GEL equal to 1 m. The color bar represents the water depth. The brown shaded areas represent the areas where the water cannot be accumulated. The white squares are zoomed areas on Nirgal Vallis' watershed (b), Jezero' watershed (c) and Gale' watershed (d). The white stars localized the Nirgal Vallis outlet (b), Jezero crater (c) and Gale crater (d).

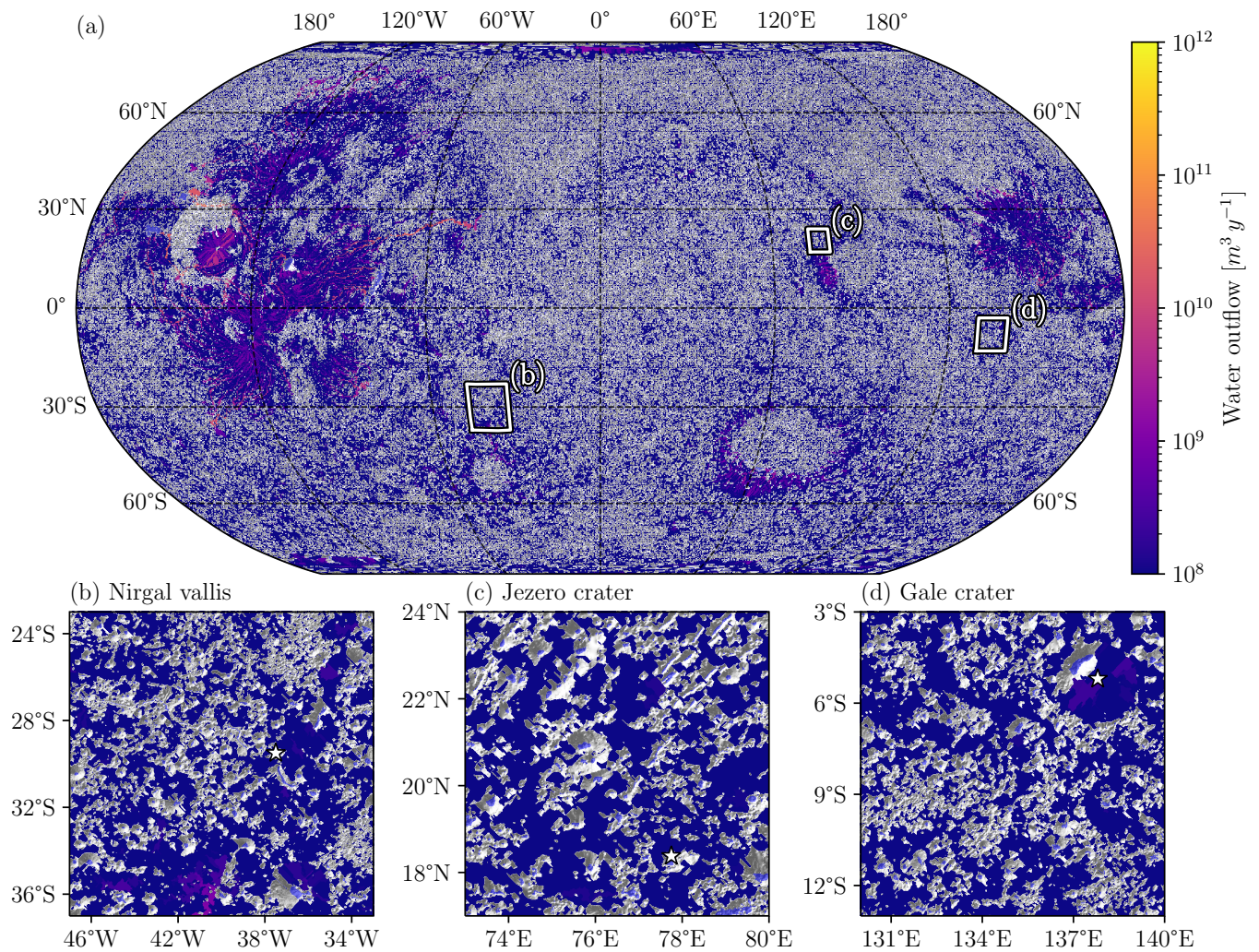


Figure D2. Water overflow at steady state with a $GEL = 1\text{ m}$ and $E = 1\text{ m}\cdot\text{y}^{-1}$. The color bar represents the water flow accumulation. The areas where there is no outflow are symbolized by white shaded areas and sky blue areas represent the watershed and lake/ocean areas. The first line of zoomed plots shows the raw output data of the hydrological model which represents the water overflow associated to the watershed area.

D2 Global Equivalent Layer of 10 m

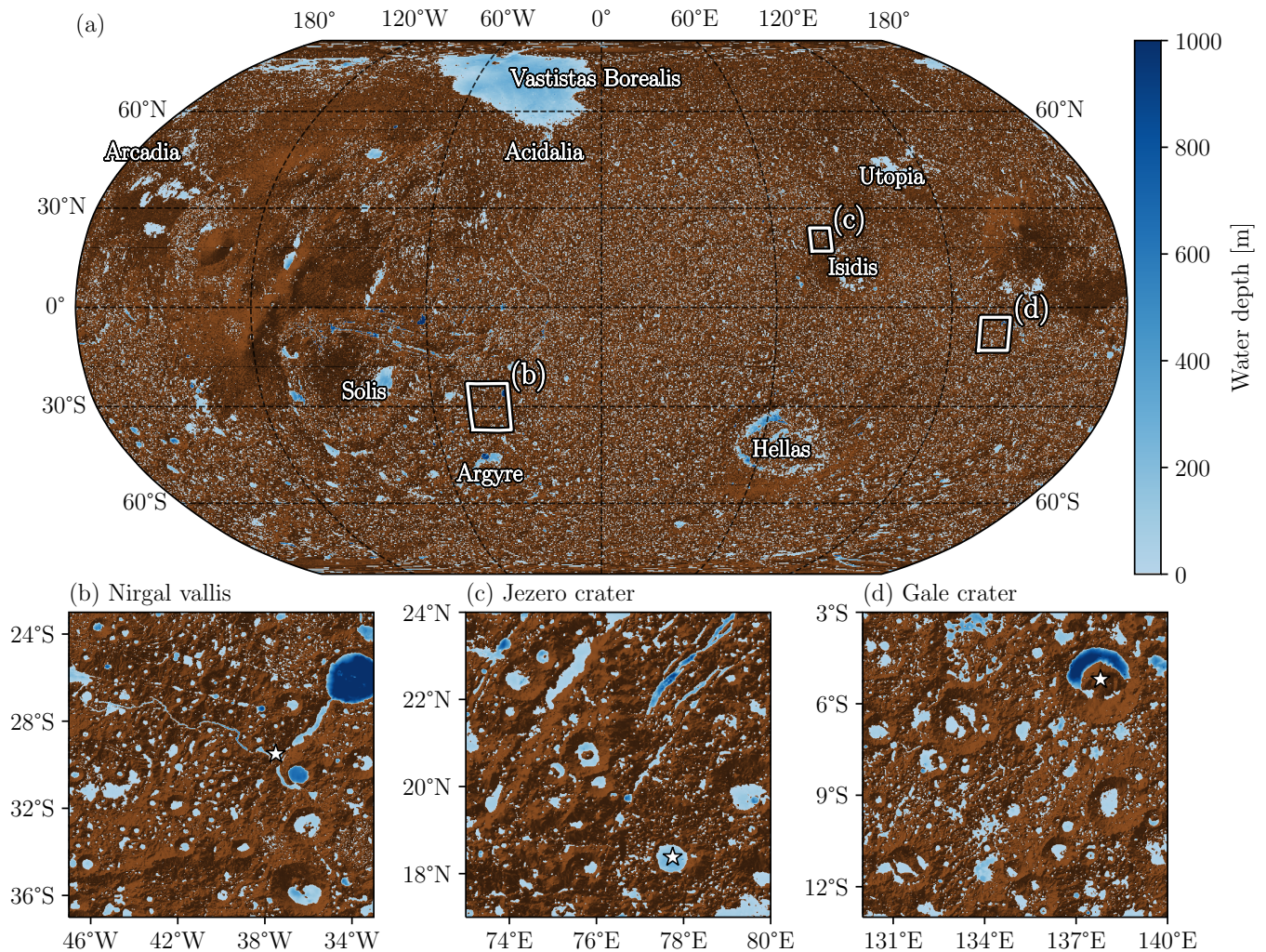


Figure D3. Distribution of water reservoirs (blue areas) at steady state with a GEL equal to 10 m. The color bar represents the water depth. The brown shaded areas represent the areas where the water cannot be accumulated. The white squares are zoomed areas on Nirgal Vallis' watershed (b), Jezero' watershed (c) and Gale' watershed (d). The white stars localized the Nirgal Vallis outlet (b), Jezero crater (c) and Gale crater (d).

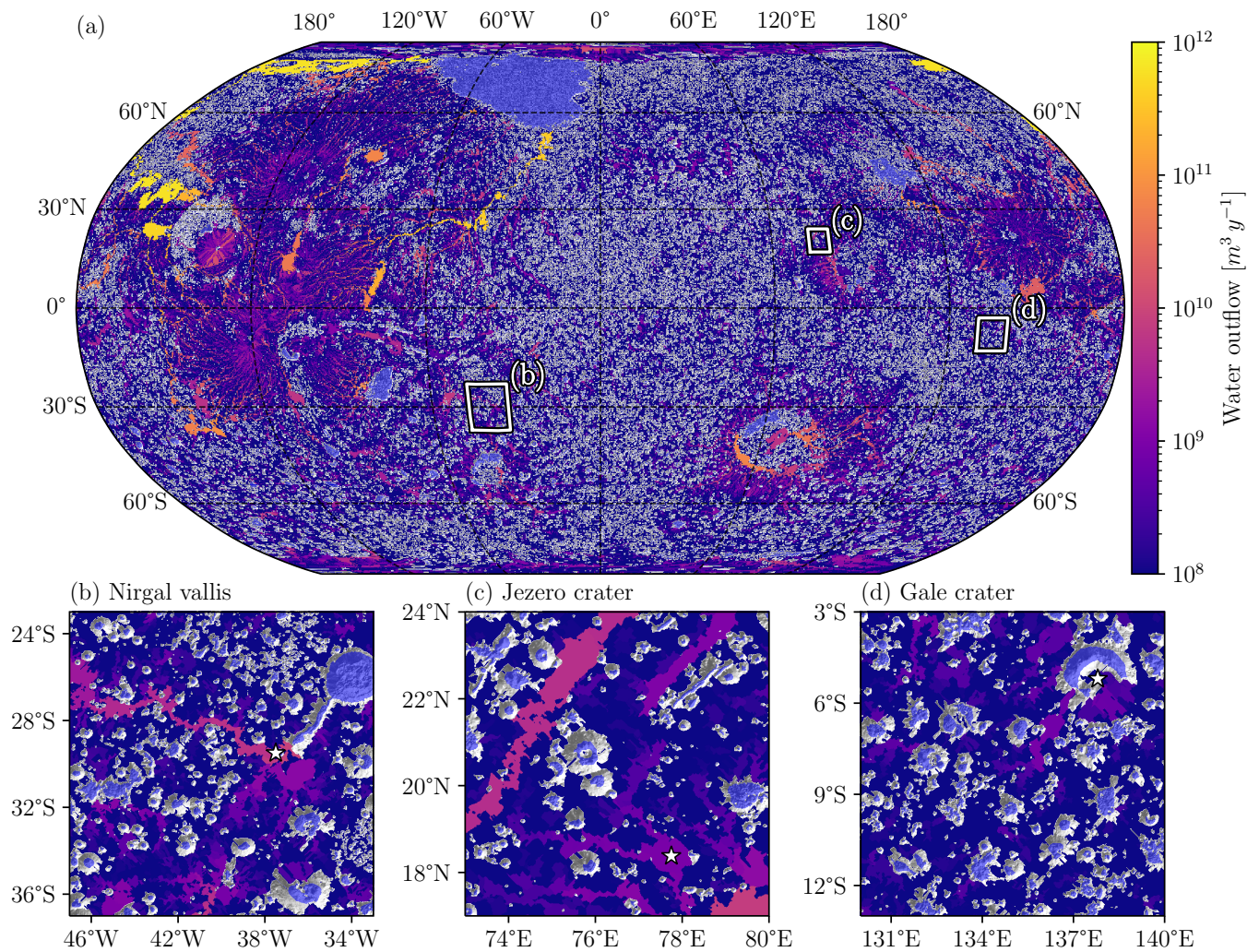


Figure D4. Water overflow at steady state with a $GEL = 10$ m and $E = 1 m.y^{-1}$. The color bar represents the water flow accumulation. The areas where there is no outflow are symbolized by white shaded areas and sky blue areas represent the watershed and lake/ocean areas. The first line of zoomed plots shows the raw output data of the hydrological model which represents the water overflow associated to the watershed area.

D3 Global Equivalent Layer of 1,000 m

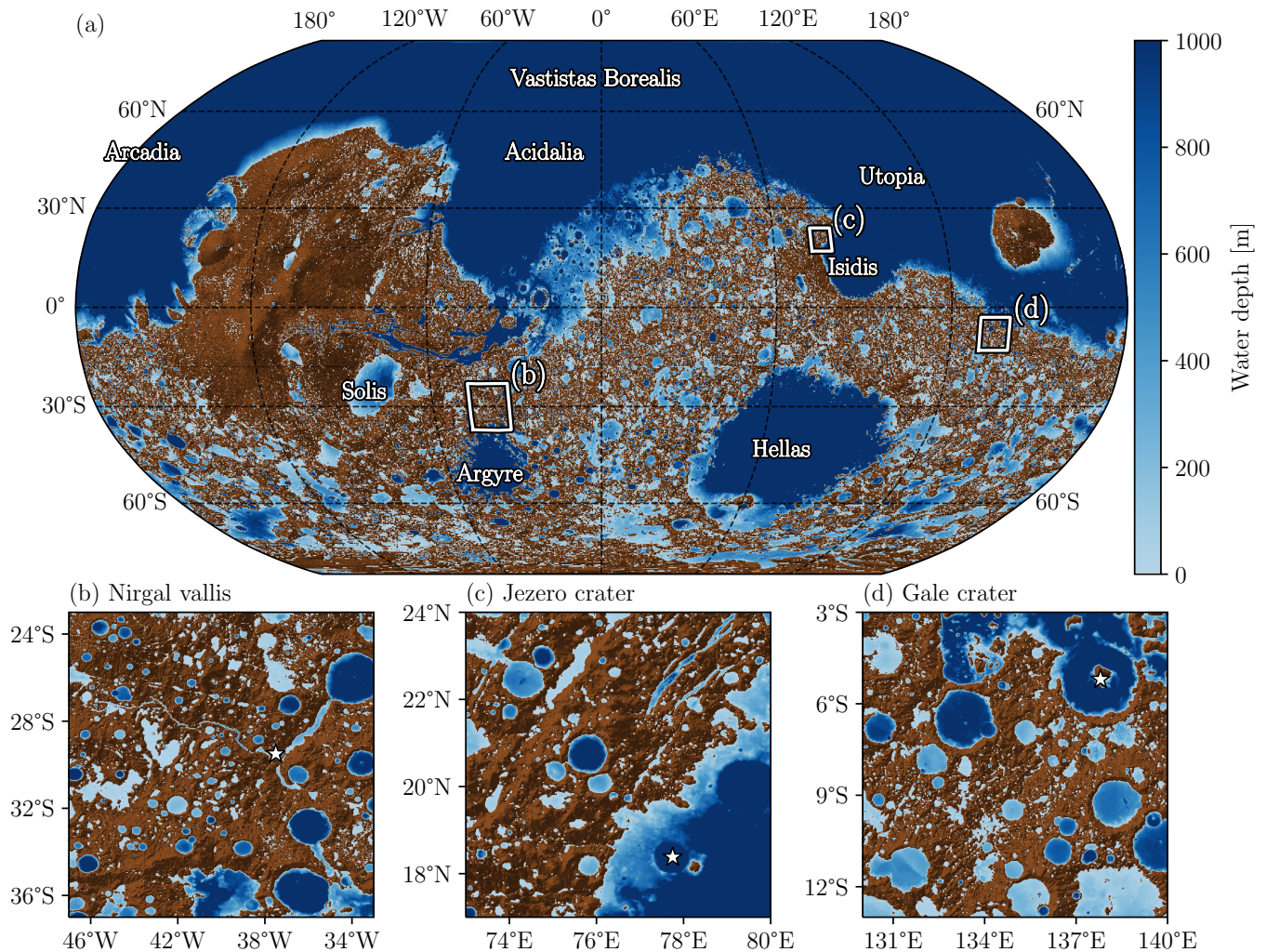


Figure D5. Distribution of water reservoirs (blue areas) at steady state with a GEL equal to 1,000 m. The color bar represents the water depth. The brown shaded areas represent the areas where the water cannot be accumulated. The white squares are zoomed areas on Nirgal Vallis' watershed (b), Jezero' watershed (c) and Gale' watershed (d). The white stars localized the Nirgal Vallis outlet (b), Jezero crater (c) and Gale crater (d).

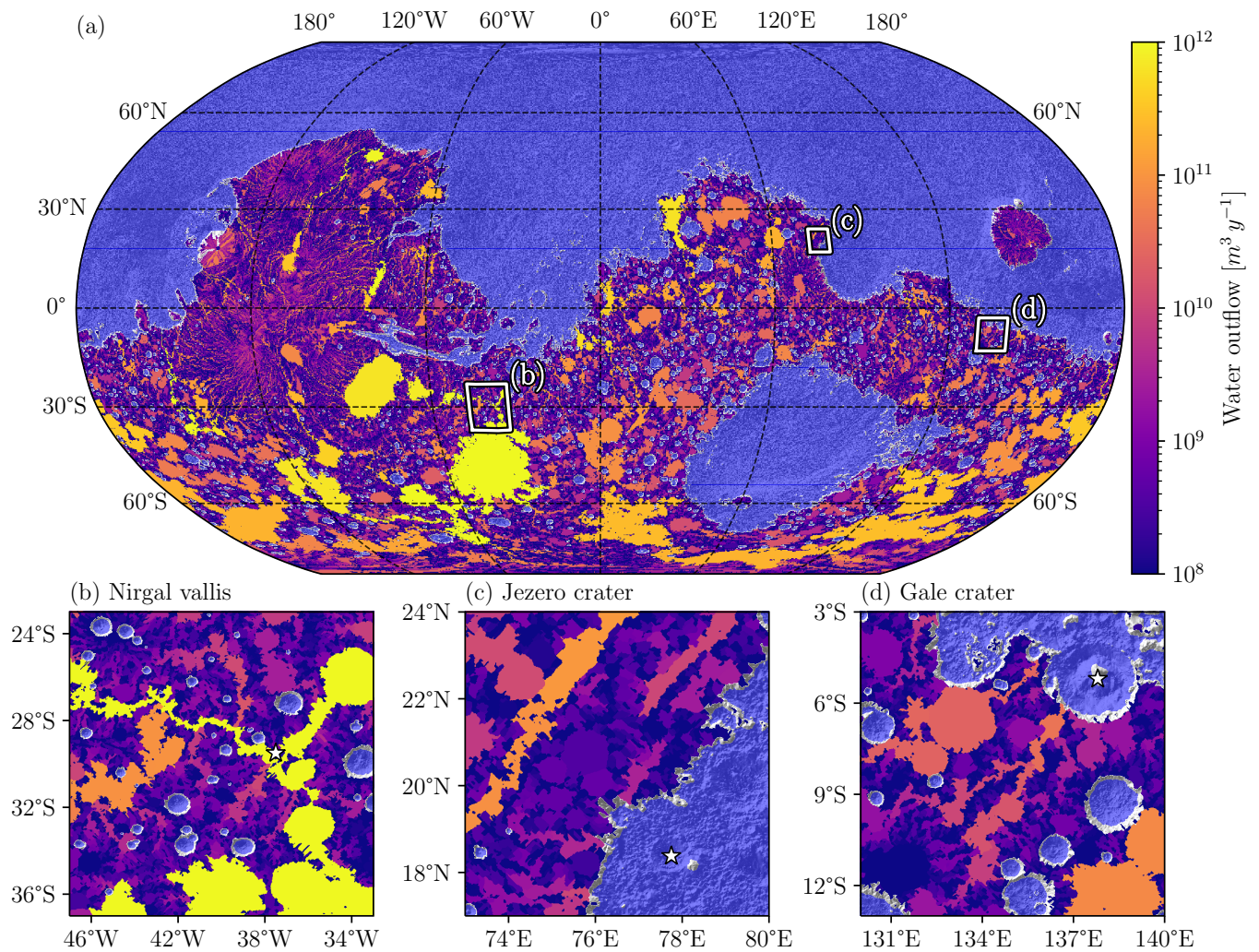


Figure D6. Water overflow at steady state with a $GEL = 1,000 \text{ m}$ and $E = 1 \text{ m.y}^{-1}$. The color bar represents the water flow accumulation. The areas where there is no outflow are symbolized by white shaded areas and sky blue areas represent the watershed and lake/ocean areas. The first line of zoomed plots shows the raw output data of the hydrological model which represents the water overflow associated to the watershed area.

Author contributions. Alexandre Gauvain: Conceptualization, Methodology, Software, Validation, Visualization, Writing - original draft preparation, Writing - review & editing. François Forget: Conceptualization, Funding acquisition, Methodology, Project administration, Supervision, Writing - review & editing. Martin Turbet: Methodology, Writing - review & editing. Jean-Baptiste Clément: Methodology, Software, Writing - review & editing. Lucas Lange : Methodology, Visualization, Writing - review & editing. Romain Vandemeulebrouck : Methodology, Software.

Competing interests. The authors declare that they have no conflict of interest.

Acknowledgements. This project has received funding from the European Research Council (ERC) under the European Union’s Horizon 2020 research and innovation program (Grant 835275) through the “Mars Through Time” project. To process the hydrological database, this study benefited from the IPSL Data and Computing Center ESPRI which is supported by CNRS, SU, CNES and Ecole Polytechnique. Simulations were done thanks to the High-Performance Computing resources of Centre Informatique National de l’Enseignement Supérieur (CINES) under the allocations n°A0140110391 and n°A0160110391 made by Grand Equipement National de Calcul Intensif (GENCI). We thank Agnes Ducharne for useful discussions.

References

- Andrews-Hanna, J. C., Zuber, M. T., Arvidson, R. E., and Wiseman, S. M.: Early Mars hydrology: Meridiani playa deposits and the sedimentary record of Arabia Terra, *Journal of Geophysical Research: Planets*, 115, <https://doi.org/10.1029/2009JE003485>, 2010.
- Barnes, R.: RichDEM: Terrain Analysis Software, <http://github.com/r-barnes/richdem>, 2016.
- Barnes, R., Lehman, C., and Mulla, D.: Priority-flood: An optimal depression-filling and watershed-labeling algorithm for digital elevation models, *Computers & Geosciences*, 62, 117–127, <https://doi.org/10.1016/j.cageo.2013.04.024>, 2014.
- Barnes, R., Callaghan, K. L., and Wickert, A. D.: Computing Water Flow through Complex Landscapes – Part 2: Finding Hierarchies in Depressions and Morphological Segmentations, 8, 431–445, <https://doi.org/10.5194/esurf-8-431-2020>, 2020.
- Barnes, R., Callaghan, K. L., and Wickert, A. D.: Computing Water Flow through Complex Landscapes – Part 3: Fill–Spill–Merge: Flow Routing in Depression Hierarchies, 9, 105–121, <https://doi.org/10.5194/esurf-9-105-2021>, 2021.
- Bartos, M.: pysheds: simple and fast watershed delineation in python, <https://doi.org/10.5281/zenodo.3822494>, 2020.
- Beck, P., Beyssac, O., Dehouck, E., Bernard, S., Pineau, M., Mandon, L., Royer, C., Clavé, E., Schröder, S., Forni, O., Francis, R., Mangold, N., Bedford, C., Broz, A., Cloutis, E., Johnson, J., Poulet, F., Fouchet, T., Quantin-Nataf, C., Pilorget, C., Rapin, W., Meslin, P.-Y., Gabriel, T., Arana, G., Madariaga, J., Brown, A., Maurice, S., Clegg, S., Gasnault, O., Cousin, A., and Wiens, R.: From hydrated silica to quartz: Potential hydrothermal precipitates found in Jezero crater, Mars, *Earth and Planetary Science Letters*, 656, 119–256, <https://doi.org/10.1016/j.epsl.2025.119256>, 2025.
- Bibring, J.-P., Langevin, Y., Mustard, J. F., Poulet, F., Arvidson, R., Gendrin, A., Gondet, B., Mangold, N., Pinet, P., Forget, F., Berthé, M., Bibring, J.-P., Gendrin, A., Gomez, C., Gondet, B., Jouglet, D., Poulet, F., Soufflot, A., Vincendon, M., Combes, M., Drossart, P., Encrenaz, T., Fouchet, T., Merchiorri, R., Belluci, G., Altieri, F., Formisano, V., Capaccioni, F., Cerroni, P., Coradini, A., Fonti, S., Korablev, O., Kottsov, V., Ignatiev, N., Moroz, V., Titov, D., Zasova, L., Loiseau, D., Mangold, N., Pinet, P., Douté, S., Schmitt, B., Sotin, C., Hauber, E., Hoffmann, H., Jaumann, R., Keller, U., Arvidson, R., Mustard, J. F., Duxbury, T., Forget, F., and Neukum, G.: Global Mineralogical and Aqueous Mars History Derived from OMEGA/Mars Express Data, 312, 400–404, <https://doi.org/10.1126/science.1122659>, 2006.
- Boatwright, B. D. and Head, J. W.: Simulating early Mars hydrology with the MARSSIM landform evolution model: New insights from an integrated system of precipitation, infiltration, and groundwater flow, *Planetary and Space Science*, 171, 17–33, <https://doi.org/10.1016/j.pss.2019.04.001>, 2019.
- Bouley, S., Ansan, V., Mangold, N., Masson, P., and Neukum, G.: Fluvial morphology of Naktong Vallis, Mars: A late activity with multiple processes, *Planetary and Space Science*, 57, 982–999, <https://doi.org/10.1016/j.pss.2009.01.015>, European Mars Science and Exploration Conference (EMSEC), 2009.
- Bouley, S., Baratoux, D., Matsuyama, I., Forget, F., Séjourné, A., Turbet, M., and Costard, F.: Late Tharsis Formation and Implications for Early Mars, *Nature*, 531, 344–347, <https://doi.org/10.1038/nature17171>, 2016.
- Callaghan, K. L. and Wickert, A. D.: Computing water flow through complex landscapes – Part 1: Incorporating depressions in flow routing using FlowFill, *Earth Surface Dynamics*, 7, 737–753, <https://doi.org/10.5194/esurf-7-737-2019>, 2019.
- Carr, M. H. and Chuang, F. C.: Martian drainage densities, *Journal of Geophysical Research: Planets*, 102, 9145–9152, <https://doi.org/10.1029/97JE00113>, 1997.
- Carr, M. H. and Clow, G. D.: Martian channels and valleys: Their characteristics, distribution, and age, *Icarus*, 48, 91–117, [https://doi.org/10.1016/0019-1035\(81\)90156-1](https://doi.org/10.1016/0019-1035(81)90156-1), 1981.

- Carr, M. H. and Head, J. W.: Martian Surface/near-Surface Water Inventory: Sources, Sinks, and Changes with Time, 42, 726–732, <https://doi.org/10.1002/2014GL062464>, 2015.
- Carr, M. H. and Malin, M. C.: Meter-Scale Characteristics of Martian Channels and Valleys, *Icarus*, 146, 366–386, <https://doi.org/10.1006/icar.2000.6428>, 2000.
- Carter, J., Loizeau, D., Mangold, N., Poulet, F., and Bibring, J.-P.: Widespread surface weathering on early Mars: A case for a warmer and wetter climate, *Icarus*, 248, 373–382, <https://doi.org/10.1016/j.icarus.2014.11.011>, 2015.
- Citron, R. I., Manga, M., and Hemingway, D. J.: Timing of oceans on Mars from shoreline deformation, 555, 643–646, <https://doi.org/10.1038/nature26144>, 2018.
- Clément, J.-B., Forget, F., Lange, L., Vos, E., Millour, E., Naar, J., and Vandemeulebrouck, R.: Investigating Long-Term Mars Climate Evolution: The Planetary Evolution Model, in: Tenth International Conference on Mars, pp. LPI Contribution No. 3007, 2024, id.3064, Pasadena, United States, <https://www.hou.usra.edu/meetings/tenthmars2024/pdf/3064.pdf>, 2024.
- Craddock, R. A. and Howard, A. D.: The case for rainfall on a warm, wet early Mars, *Journal of Geophysical Research: Planets*, 107, 21–21–36, <https://doi.org/10.1029/2001JE001505>, 2002.
- Dai, A. and Trenberth, K. E.: Estimates of Freshwater Discharge from Continents: Latitudinal and Seasonal Variations, *Journal of Hydrometeorology*, 3, 660 – 687, [https://doi.org/10.1175/1525-7541\(2002\)003<0660:EOFDfC>2.0.CO;2](https://doi.org/10.1175/1525-7541(2002)003<0660:EOFDfC>2.0.CO;2), 2002.
- Di Achille, G. and Hynek, B. M.: Ancient Ocean on Mars Supported by Global Distribution of Deltas and Valleys, 3, 459–463, <https://doi.org/10.1038/ngeo891>, 2010.
- Ehlmann, B. L., Mustard, J. F., Murchie, S. L., Bibring, J.-P., Meunier, A., Fraeman, A. A., and Langevin, Y.: Subsurface water and clay mineral formation during the early history of Mars, 479, 53–60, <https://doi.org/10.1038/nature10582>, 2011.
- Fan, Y. and Miguez-Macho, G.: A Simple Hydrologic Framework for Simulating Wetlands in Climate and Earth System Models, 37, 253–278, <https://doi.org/10.1007/s00382-010-0829-8>, 2011.
- Fassett, C. I. and Head, J. W.: Fluvial sedimentary deposits on Mars: Ancient deltas in a crater lake in the Nili Fossae region, *Geophysical Research Letters*, 32, <https://doi.org/10.1029/2005GL023456>, 2005.
- Fassett, C. I. and Head, J. W.: Valley Network-Fed, Open-Basin Lakes on Mars: Distribution and Implications for Noachian Surface and Subsurface Hydrology, 198, 37–56, <https://doi.org/10.1016/j.icarus.2008.06.016>, 2008.
- Forget, F., Clement, J. B., Gauvain, A., Lange, L., Luo, Y., Maurice, M., Naar, J., Pierron, T., Vos, E., Lefevre, F., Turbet, M., Spiga, A., and Millour, E.: The “Mars Through Time” Project: Climate Modelling of the Evolution of the Environment and Surface of Mars, in: LPI Contributions, vol. 3007 of *LPI Contributions*, p. 3546, <https://www.hou.usra.edu/meetings/tenthmars2024/pdf/3546.pdf>, 2024.
- Freeman, T.: Calculating catchment area with divergent flow based on a regular grid, *Computers & Geosciences*, 17, 413–422, [https://doi.org/10.1016/0098-3004\(91\)90048-I](https://doi.org/10.1016/0098-3004(91)90048-I), 1991.
- Gaillaton, B., Steer, P., Davy, P., Schwanghart, W., and Bernard, T.: GraphFlood 1.0: an efficient algorithm to approximate 2D hydrodynamics for landscape evolution models, *Earth Surface Dynamics*, 12, 1295–1313, <https://doi.org/10.5194/esurf-12-1295-2024>, 2024.
- Gauvain, A.: A Global High-Resolution Hydrological Model to Simulate the Dynamics of Surface Liquid Reservoirs: Application on Mars (Model and Datasets), <https://doi.org/10.5281/zenodo.17208793>, 2025.
- Goudge, T. A., Fassett, C. I., Head, J. W., Mustard, J. F., and Aureli, K. L.: Insights into Surface Runoff on Early Mars from Paleolake Basin Morphology and Stratigraphy, 44, 419–422, <https://doi.org/10.1130/G37734.1>, 2016.
- Grau Galofre, A., Jellinek, A. M., and Osinski, G. R.: Valley Formation on Early Mars by Subglacial and Fluvial Erosion, *Nature Geoscience*, 13, 663–668, <https://doi.org/10.1038/s41561-020-0618-x>, 2020.

- Harrison, K. P. and Grimm, R. E.: Groundwater-controlled valley networks and the decline of surface runoff on early Mars, *Journal of Geophysical Research: Planets*, 110, <https://doi.org/10.1029/2005JE002455>, 2005.
- Head, J. W., Hiesinger, H., Ivanov, M. A., Kreslavsky, M. A., Pratt, S., and Thomson, B. J.: Possible Ancient Oceans on Mars: Evidence from Mars Orbiter Laser Altimeter Data, *Science*, 286, 2134–2137, <https://doi.org/10.1126/science.286.5447.2134>, 1999.
- Hiatt, E., Shadab, M. A., Gulick, S. P., Goudge, T. A., and Hesse, M. A.: Limited recharge of the southern highlands aquifer on early Mars, *Icarus*, 408, 115–174, <https://doi.org/10.1016/j.icarus.2023.115774>, 2024.
- Hoke, M. R., Hynes, B. M., and Tucker, G. E.: Formation timescales of large Martian valley networks, *Earth and Planetary Science Letters*, 312, 1–12, <https://doi.org/10.1016/j.epsl.2011.09.053>, 2011.
- Horvath, D. G. and Andrews-Hanna, J. C.: Reconstructing the past climate at Gale crater, Mars, from hydrological modeling of late-stage lakes, *Geophysical Research Letters*, 44, 8196–8204, <https://doi.org/10.1002/2017GL074654>, 2017.
- Horvath, D. G. and Andrews-Hanna, J. C.: The hydrology and climate of Mars during the sedimentary infilling of Gale crater, *Earth and Planetary Science Letters*, 568, 117–132, <https://doi.org/10.1016/j.epsl.2021.117032>, 2021.
- Houston, J.: Evaporation in the Atacama Desert: An empirical study of spatio-temporal variations and their causes, *Journal of Hydrology*, 330, 402–412, <https://doi.org/10.1016/j.jhydrol.2006.03.036>, 2006.
- Howard, A. D.: Simulating the Development of Martian Highland Landscapes through the Interaction of Impact Cratering, Fluvial Erosion, and Variable Hydrologic Forcing, 91, 332–363, <https://doi.org/10.1016/j.geomorph.2007.04.017>, 2007.
- Hynes, B. M., Beach, M., and Hoke, M. R. T.: Updated Global Map of Martian Valley Networks and Implications for Climate and Hydrologic Processes, 115, <https://doi.org/10.1029/2009JE003548>, 2010.
- Irwin, Rossman P., I., Craddock, R. A., and Howard, A. D.: Interior channels in Martian valley networks: Discharge and runoff production, *Geology*, 33, 489–492, <https://doi.org/10.1130/G21333.1>, 2005a.
- Irwin, Rossman P., I., Howard, A. D., Craddock, R. A., and Moore, J. M.: An intense terminal epoch of widespread fluvial activity on early Mars: 2. Increased runoff and paleolake development, *Journal of Geophysical Research: Planets*, 110, <https://doi.org/10.1029/2005JE002460>, 2005b.
- Irwin III, R. P., Howard, A. D., and Maxwell, T. A.: Geomorphology of Ma'adim Vallis, Mars, and associated paleolake basins, *Journal of Geophysical Research: Planets*, 109, <https://doi.org/10.1029/2004JE002287>, 2004.
- Ivanov, M., Erkeling, G., Hiesinger, H., Bernhardt, H., and Reiss, D.: Topography of the Deuteronilus Contact on Mars: Evidence for an Ancient Water/Mud Ocean and Long-Wavelength Topographic Readjustments, *Planetary and Space Science*, 144, 49–70, <https://doi.org/10.1016/j.pss.2017.05.012>, 2017.
- Jakosky, B. M. and Hallis, L. J.: Fate of an Earth-Like Water Inventory on Mars, *Journal of Geophysical Research: Planets*, 129, e2023JE008159, <https://doi.org/10.1029/2023JE008159>, e2023JE008159 2023JE008159, 2024.
- Kamada, A., Kuroda, T., Kasaba, Y., Terada, N., Nakagawa, H., and Toriumi, K.: A coupled atmosphere–hydrosphere global climate model of early Mars: A "cool and wet" scenario for the formation of water channels, *Icarus*, 338, 113–167, <https://doi.org/10.1016/j.icarus.2019.113567>, 2020.
- Kamada, A., Kuroda, T., Kasaba, Y., Terada, N., and Nakagawa, H.: Global climate and river transport simulations of early Mars around the Noachian and Hesperian boundary, *Icarus*, 368, 114–168, <https://doi.org/10.1016/j.icarus.2021.114618>, 2021.
- Kite, E. S., Mayer, D. P., Wilson, S. A., Davis, J. M., Lucas, A. S., and de Quay, G. S.: Persistence of intense, climate-driven runoff late in Mars history, *Science Advances*, 5, eaav7710, <https://doi.org/10.1126/sciadv.aav7710>, 2019.

- Li, J., Liu, H., Meng, X., Duan, D., Lu, H., Zhang, J., Zhang, F., Elsworth, D., Cardenas, B. T., Manga, M., Zhou, B., and Fang, G.: Ancient ocean coastal deposits imaged on Mars, *Proceedings of the National Academy of Sciences*, 122, e2422213122, <https://doi.org/10.1073/pnas.2422213122>, 2025.
- Liu, D., Cheng, W., Qian, Z., Liu, J., Liu, J., and Wang, X.: A global catalog of Martian impact craters with actual boundaries and degradation states, *International Journal of Applied Earth Observation and Geoinformation*, 131, 103 952, <https://doi.org/10.1016/j.jag.2024.103952>, 2024.
- Luo, W. and Howard, A. D.: Computer simulation of the role of groundwater seepage in forming Martian valley networks, *Journal of Geophysical Research: Planets*, 113, <https://doi.org/10.1029/2007JE002981>, 2008.
- Malin, M. C. and Carr, M. H.: Groundwater Formation of Martian Valleys, *Nature*, 397, 589–591, <https://doi.org/10.1038/17551>, 1999.
- Malin, M. C. and Edgett, K. S.: Sedimentary Rocks of Early Mars, 290, 1927–1937, <https://doi.org/10.1126/science.290.5498.1927>, 2000.
- Mangold, N., Quantin, C., Ansan, V., Delacourt, C., and Allemand, P.: Evidence for Precipitation on Mars from Dendritic Valleys in the Valles Marineris Area, *Science*, 305, 78–81, <https://doi.org/10.1126/science.1097549>, 2004.
- Mangold, N., Mangold, N., Mangold, N., Howard, A. D., and Howard, A. D.: Outflow channels with deltaic deposits in Ismenius Lacus, Mars, *Icarus*, <https://doi.org/10.1016/j.icarus.2013.05.040>, 2013.
- Matsubara, Y., Howard, A. D., and Drummond, S. A.: Hydrology of Early Mars: Lake Basins, 116, E04 001, <https://doi.org/10.1029/2010JE003739>, 2011.
- Matsubara, Y., Howard, A. D., and Gochenour, J. P.: Hydrology of Early Mars: Valley Network Incision: HYDROLOGY OF EARLY MARS: VALLEY INCISION, 118, 1365–1387, <https://doi.org/10.1002/jgre.20081>, 2013.
- Morgan, A. M.: New maximum constraints on the era of martian valley network formation, *Earth and Planetary Science Letters*, 626, 118 509, <https://doi.org/10.1016/j.epsl.2023.118509>, 2024.
- Morgan, G. A. and Head, J. W.: Sinton crater, Mars: Evidence for impact into a plateau icefield and melting to produce valley networks at the Hesperian–Amazonian boundary, *Icarus*, 202, 39–59, <https://doi.org/10.1016/j.icarus.2009.02.025>, 2009.
- Neumann, G. A., Rowlands, D. D., Lemoine, F. G., Smith, D. E., and Zuber, M. T.: Crossover analysis of Mars Orbiter Laser Altimeter data, *Journal of Geophysical Research: Planets*, 106, 23 753–23 768, <https://doi.org/10.1029/2000JE001381>, 2001.
- Noel, S. A., Ault, A. C., Buckmaster, D. R., and Krogmeier, J. V.: A Rainfall-Based, Sequential Depression-Filling Algorithm and Assessments on a Watershed in Northeastern Indiana, USA, *Journal of Advances in Modeling Earth Systems*, 13, e2020MS002 362, <https://doi.org/10.1029/2020MS002362>, e2020MS002362 2020MS002362, 2021.
- O’Callaghan, J. F. and Mark, D. M.: The extraction of drainage networks from digital elevation data, *Computer Vision, Graphics, and Image Processing*, 28, 323–344, [https://doi.org/10.1016/S0734-189X\(84\)80011-0](https://doi.org/10.1016/S0734-189X(84)80011-0), 1984.
- Palucis, M. C., Dietrich, W. E., Hayes, A. G., Williams, R. M. E., Gupta, S., Mangold, N., Newsom, H., Hardgrove, C., Calef III, F., and Sumner, D. Y.: The origin and evolution of the Peace Vallis fan system that drains to the Curiosity landing area, Gale Crater, Mars, *Journal of Geophysical Research: Planets*, 119, 705–728, <https://doi.org/10.1002/2013JE004583>, 2014.
- Perron, J. T., Mitrovica, J. X., Manga, M., Matsuyama, I., and Richards, M. A.: Evidence for an Ancient Martian Ocean in the Topography of Deformed Shorelines, *Nature*, 447, 840–843, <https://doi.org/10.1038/nature05873>, 2007.
- Phillips, R. J., Zuber, M. T., Solomon, S. C., Golombek, M. P., Jakosky, B. M., Banerdt, W. B., Smith, D. E., Williams, R. M. E., Hynes, B. M., Aharonson, O., and II, S. A. H.: Ancient Geodynamics and Global-Scale Hydrology on Mars, *Science*, 291, 2587–2591, <https://doi.org/10.1126/science.1058701>, 2001.

- Robbins, S. J. and Hynek, B. M.: A new global database of Mars impact craters ≥ 1 km: 1. Database creation, properties, and parameters, *Journal of Geophysical Research: Planets*, 117, <https://doi.org/10.1029/2011JE003966>, 2012.
- Salles, T., Mallard, C., and Zahirovic, S.: gospl: Global Scalable Paleo Landscape Evolution, *Journal of Open Source Software*, 5, 2804, <https://doi.org/10.21105/joss.02804>, 2020.
- Salles, T., Husson, L., Rey, P., Mallard, C., Zahirovic, S., Boggiani, B. H., Coltice, N., and Arnould, M.: Hundred million years of landscape dynamics from catchment to global scale, *Science*, 379, 918–923, <https://doi.org/10.1126/science.add2541>, 2023.
- Scheller, E. L., Ehlmann, B. L., Hu, R., Adams, D. J., and Yung, Y. L.: Long-term drying of Mars by sequestration of ocean-scale volumes of water in the crust, *Science*, 372, 56–62, <https://doi.org/10.1126/science.abc7717>, 2021.
- Seybold, H. J., Kite, E., and Kirchner, J. W.: Branching geometry of valley networks on Mars and Earth and its implications for early Martian climate, *Science Advances*, 4, eaar6692, <https://doi.org/10.1126/sciadv.aar6692>, 2018.
- Shadab, M. A., Hiatt, E., Bahia, R. S., Bohacek, E. V., Steinmann, V., and Hesse, M. A.: Infiltration Dynamics on Early Mars: Geomorphic, Climatic, and Water Storage Implications, *Geophysical Research Letters*, 52, e2024GL111939, <https://doi.org/10.1029/2024GL111939>, e2024GL111939 2024GL111939, 2025.
- Sholes, S. F., Dickeson, Z. I., Montgomery, D. R., and Catling, D. C.: Where are Mars' Hypothesized Ocean Shorelines? Large Lateral and Topographic Offsets Between Different Versions of Paleoshoreline Maps, *Journal of Geophysical Research: Planets*, 126, e2020JE006486, <https://doi.org/10.1029/2020JE006486>, e2020JE006486 2020JE006486, 2021.
- Shook, K., Spiteri, R. J., Pomeroy, J. W., Liu, T., and Sharomi, O.: WDPM: the Wetland DEM Ponding Model, *Journal of Open Source Software*, 6, 2276, <https://doi.org/10.21105/joss.02276>, 2021.
- Smith, D. E., Zuber, M. T., Solomon, S. C., Phillips, R. J., Head, J. W., Garvin, J. B., Banerdt, W. B., Muhleman, D. O., Pettengill, G. H., Neumann, G. A., Lemoine, F. G., Abshire, J. B., Aharonson, O., David, C., null, Hauck, S. A., Ivanov, A. B., McGovern, P. J., Zwally, H. J., and Duxbury, T. C.: The Global Topography of Mars and Implications for Surface Evolution, *Science*, 284, 1495–1503, <https://doi.org/10.1126/science.284.5419.1495>, 1999.
- Smith, D. E., Zuber, M. T., Frey, H. V., Garvin, J. B., Head, J. W., Muhleman, D. O., Pettengill, G. H., Phillips, R. J., Solomon, S. C., Zwally, H. J., Banerdt, W. B., Duxbury, T. C., Golombek, M. P., Lemoine, F. G., Neumann, G. A., Rowlands, D. D., Aharonson, O., Ford, P. G., Ivanov, A. B., Johnson, C. L., McGovern, P. J., Abshire, J. B., Afzal, R. S., and Sun, X.: Mars Orbiter Laser Altimeter: Experiment summary after the first year of global mapping of Mars, *Journal of Geophysical Research: Planets*, 106, 23 689–23 722, <https://doi.org/10.1029/2000JE001364>, 2001.
- Sood, A., Sood, A., Smakhtin, V., and Smakhtin, V. U.: Global hydrological models: a review, *Hydrological Sciences Journal-journal Des Sciences Hydrologiques*, <https://doi.org/10.1080/02626667.2014.950580>, 2015.
- Stucky de Quay, G., Goudge, T. A., and Fassett, C. I.: Precipitation and aridity constraints from paleolakes on early Mars, *Geology*, 48, 1189–1193, <https://doi.org/10.1130/G47886.1>, 2020.
- Tanaka, K. L., Skinner, J. A., Dohm, J. M., Iii, R. P. I., Kolb, E. J., Fortezzo, C. M., Platz, T., Michael, G. G., and Hare, T. M.: Geologic Map of Mars, Tech. Rep. 3292, U.S. Geological Survey, ISSN 2329-132X, <https://doi.org/10.3133/sim3292>, 2014.
- Turbet, M. and Forget, F.: 3-D Global modelling of the early martian climate under a dense CO₂+H₂ atmosphere and for a wide range of surface water inventories, <https://arxiv.org/abs/2103.10301>, 2021.
- Turbet, M., Forget, F., Head, J. W., and Wordsworth, R.: 3D modelling of the climatic impact of outflow channel formation events on early Mars, *Icarus*, 288, 10–36, <https://doi.org/10.1016/j.icarus.2017.01.024>, 2017.

- van Jaarsveld, B., Wanders, N., Sutanudjaja, E. H., Hoch, J., Droppers, B., Janzing, J., van Beek, R. L. P. H., and Bierkens, M. F. P.: A first attempt to model global hydrology at hyper-resolution, *Earth System Dynamics*, 16, 29–54, <https://doi.org/10.5194/esd-16-29-2025>, 2025.
- Verkaik, J., Sutanudjaja, E. H., Oude Essink, G. H. P., Lin, H. X., and Bierkens, M. F. P.: GLOBGM v1.0: a parallel implementation of a 30 arcsec PCR-GLOBWB-MODFLOW global-scale groundwater model, *Geoscientific Model Development*, 17, 275–300, <https://doi.org/10.5194/gmd-17-275-2024>, 2024.
- Villanueva, G. L., Mumma, M. J., Novak, R. E., Käüfl, H. U., Hartogh, P., Encrenaz, T., Tokunaga, A., Khayat, A., and Smith, M. D.: Strong Water Isotopic Anomalies in the Martian Atmosphere: Probing Current and Ancient Reservoirs, 348, 218–221, <https://doi.org/10.1126/science.aaa3630>, 2015.
- Williams, R. M. E. and Phillips, R. J.: Morphometric measurements of martian valley networks from Mars Orbiter Laser Altimeter (MOLA) data, *Journal of Geophysical Research: Planets*, 106, 23 737–23 751, <https://doi.org/10.1029/2000JE001409>, 2001.
- Wordsworth, R., Forget, F., Millour, E., Head, J., Madeleine, J.-B., and Charnay, B.: Global modelling of the early martian climate under a denser CO₂ atmosphere: Water cycle and ice evolution, *Icarus*, 222, 1–19, <https://doi.org/10.1016/j.icarus.2012.09.036>, 2013.
- Wordsworth, R., Kerber, L., Pierrehumbert, R. T., Forget, F., and Head, J. W.: Comparison of “warm and wet” and “cold and icy” scenarios for early Mars in a 3-D climate model, *Journal of Geophysical Research: Planets*, 120, 1201–1219, <https://doi.org/10.1002/2015JE004787>, 2015.
- Zuber, M. T.: Oceans on Mars formed early, *Nature*, <https://doi.org/10.1038/d41586-018-03415-x>, 2018.